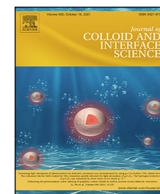




Contents lists available at ScienceDirect

Journal of Colloid and Interface Science

journal homepage: www.elsevier.com/locate/jcis

Regular Article

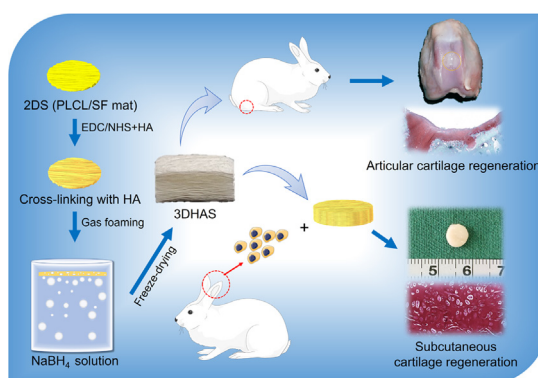
Three-dimensional porous gas-foamed electrospun nanofiber scaffold for cartilage regeneration

Yujie Chen^{a,1}, Wei Xu^{b,c,d,1}, Muhammad Shafiq^{a,e,*}, Jincheng Tang^{b,c,d}, Junxiang Hao^{b,c,d}, Xianrui Xie^a, Zhengchao Yuan^a, Xianghao Xiao^a, Yu Liu^{b,c,d,*}, Xiumei Mo^{a,*}^a Shanghai Engineering Research Center of Nano-Biomaterials and Regenerative Medicine, College of Chemistry, Chemical Engineering and Biotechnology, Donghua University, Songjiang, Shanghai 201600, China^b Research Institute of Plastic Surgery, Wei Fang Medical College, Weifang 261000, China^c National Tissue Engineering Center of China, Minhang, Shanghai 201100, China^d Shanghai Key Laboratory of Tissue Engineering, Department of Plastic and Reconstructive Surgery, Shanghai 9th People's Hospital, Shanghai Stem Cell Institute, Shanghai Jiao Tong University School of Medicine, Huangpu, Shanghai 200001, China^e Department of Health Professional Technologies (DHPT), Faculty of Allied Health Sciences, The University of Lahore (UOL), Lahore 54000, Pakistan

HIGHLIGHTS

- 3D hyaluronic acid (HA) cross-linked gas foamed scaffolds (3DHAS) were obtained.
- 3DHAS possessed stable and enhanced mechanical properties.
- Gas foamed scaffolds exhibited good biocompatibility *in vitro*.
- Gas foamed scaffolds induced neocartilage regeneration *in vivo*.
- Gas foamed scaffolds repaired articular cartilage defects in rabbits model *in vivo*.

GRAPHICAL ABSTRACT



ARTICLE INFO

Article history:

Received 26 April 2021

Revised 7 June 2021

Accepted 10 June 2021

Available online 14 June 2021

Keywords:

Electrospun

Nanofiber

Gas foaming

Three-dimensional scaffolds

Cell infiltration

Cartilage tissue engineering

Hyaluronic acid

ABSTRACT

To achieve optimal functional recovery of articular cartilage, scaffolds with nanofibrous structure and biological function have been widely pursued. In this study, two-dimensional electrospun poly(L-lactide-co-ε-caprolactone)/silk fibroin (PLCL/SF) scaffolds (2DS) were fabricated by dynamic liquid support (DLS) electrospinning system, and then cross-linked with hyaluronic acid (HA) to further mimic the microarchitecture of native cartilage. Subsequently, three-dimensional PLCL/SF scaffolds (3DS) and HA-crosslinked three-dimensional scaffolds (3DHAS) were successfully fabricated by *in situ* gas foaming and freeze-drying. 3DHAS exhibited better mechanical properties than that of the 3DS. Moreover, all scaffolds exhibited excellent biocompatibility *in vitro*. 3DHAS showed better proliferation and phenotypic maintenance of chondrocytes as compared to the other scaffolds. Histological analysis of cell-scaffold constructs explanted 8 weeks after implantation demonstrated that both 3DS and 3DHAS scaffolds formed cartilage-like tissues, and the cartilage lacuna formed in 3DHAS scaffolds was more mature. Moreover, the reparative capacity of scaffolds was discerned after implantation in the full-thickness articular cartilage model in rabbits for up to 12 weeks. The macroscopic and histological results exhibited

* Corresponding authors at: Shanghai Engineering Research Center of Nano-Biomaterials and Regenerative Medicine, College of Chemistry, Chemical Engineering and Biotechnology, Donghua University, Songjiang, Shanghai 201600, China (M. Shafiq, X. Mo). Research Institute of Plastic Surgery, Wei Fang Medical College, Weifang 261000, China (Y. Liu).

E-mail addresses: shafiqdr786@yahoo.com (M. Shafiq), yuliu1211@163.com (Y. Liu), xmm@dhu.edu.cn (X. Mo).

¹ These authors contributed equally to this work.

<https://doi.org/10.1016/j.jcis.2021.06.067>

0021-9797/© 2021 Elsevier Inc. All rights reserved.

typical cartilage-like character and well-integrated boundary between 3DHAS scaffolds and the host tissues. Collectively, biomimetic 3DHAS scaffolds may be promising candidates for cartilage tissue regeneration applications.

© 2021 Elsevier Inc. All rights reserved.

1. Introduction

The degeneration of articular cartilage is a widely-occurring joint disease and is a leading cause of disability, affecting millions of people world-wide. Being devoid of blood vessels and an innervation network, mature articular cartilage possesses poor regenerative capability [1]. Untreated cartilage defects may cause osteoarthritis, thus affecting the quality of life of an individual as well as the society. Current treatment modalities for cartilage degeneration include microfracture surgery, implantation of autografts, and transplantation of autologous chondrocytes [2]. However, these options are often unsatisfactory, which may lead to drawbacks, such as complex processing, high cost, lack of appropriate donors, and donor-site associated infection risks [3]. To circumvent these limitations, tissue-engineered scaffolds have been put forwarded [4].

The essential requirements of a scaffold for cartilage tissue engineering (CTE) include biomimetic architecture, stable mechanical performance and good cytocompatibility. While different methods can be employed for the fabrication of scaffolds for CTE, including salt-leaching, freeze-drying, and electrospinning, the latter is a versatile and robust technique, which has been widely exploited for fabricating extracellular matrix (ECM)-mimicking scaffolds. This is due to the high surface-to-volume ratio of nanofibers, less cost, simple-to-establish process, and a freedom in choosing the spinnable materials [5]. However, normal electrospinning typically generates two-dimensional (2D) membranes with tightly-packed layers due to the sheet-like assembly of fibers, which impedes cellular infiltration into scaffolds. Dynamic liquid support (DLS) electrospinning system offers several advantages over conventional electrospinning for the direct fabrication of scaffolds with the high porosity and pore size [6]. In a DLS electrospinning system, nanofibers are twisted, rearranged and stacked together to form yarns. This results into the distinct features of nanofiber mats, including an aligned microstructure, micropores, high porosity, and a hydrophilic surface. Several reports have shown that nanoyarn scaffolds can promote cell proliferation and migration. These scaffolds have previously been exploited for vascular regeneration and the treatment of the stress urinary incontinence [7,8]. However, DLS electrospinning system still results into the membranes with limited thickness and a relatively dense structure, which cannot meet the optimal conditions for cellular infiltration. Therefore, the post-treatment of electrospun scaffolds is often needed to afford scaffolds with the porous 3D-like nanostructure. These approaches include the self-assembly of short fibers [9,10], 3D printing [11] electrospinning [12] and origami and cell sheet engineering [13]. Despite improvements in the porosity and pore size of electrospun scaffolds, the lengthy and time-consuming procedures of afore-mentioned post-treatment techniques hamper the clinical translation of scaffolds. Gas foaming, which either utilizes gas bubbles generated *in situ* via a chemical reaction (e.g., the decomposition of sodium borohydride, NaBH₄) or the addition of an inert gas has been leveraged to fabricate ECM-mimicking 3D-like porous scaffolds [14,15]. Unlike 2D nanofibrous mats, 3D-like gas foamed scaffolds retain nanotopographical cues along with a multi-layered structure, which may facilitate cellular infiltration and tissue regeneration [16,17].

Previously, biomaterials designed for 3D gas foamed scaffolds mainly focused on synthetic polymers, including polycaprolactone (PCL), poly(vinylene difluoride) (PVDF), and nylon. However, these materials exhibit a hydrophobic nature and lack cell recognition cues [18–20]. Hybrid scaffolds consisting of natural and synthetic polymers may offer an alternative platform for CTE due to their better biocompatibility and mechanical properties than that of the scaffolds fabricated either from natural or synthetic polymers. In a seminal study, a layered nanofiber sponge composed of chitosan and polyvinyl alcohol (PVA) was proposed as a wound-healing and an hemostatic agent [21]. Yet in another study, a polylactic acid (PLA)/silk fibroin nanofiber sponge was used as a filler for the nerve conduits [22]. However, to the best of the authors knowledge, the gas foamed scaffolds have not yet been investigated for the regeneration of the articular cartilage. Gas-foamed scaffolds are required to meet the following requirements: 1) mimicking 3D-like microenvironment of native cartilage, 2) achieving stable mechanical properties, 3) bioactivity for cell infiltration and growth, and 4) the deposition of ECM components. Hyaluronic acid (HA), a glycosaminoglycan that is found in the cartilaginous ECM, is well-known to promote chondrogenesis and has been widely exploited for cartilage regeneration [23,24]. The cross-linked HA shows excellent elasticity and mechanical stability and is considered as an ideal bioactive source to reinforce gas foamed scaffolds for cartilage regeneration. HA could be incorporated into other matrices to improve their biomechanical and physiological properties [25,26].

The objective of this study is therefore to design 3D HA-crosslinked PLCL/SF scaffolds (3DHAS) and to evaluate the potential of the 3D gas foamed electrospun scaffolds for cartilage regeneration for the first time. Consequently, 2D PLCL/SF nanofibrous scaffolds (2DS) were fabricated by using DLS electrospinning system, crosslinked with the HA, and then submerged into sodium borohydride (NaBH₄) solution to afford fluffy 3DHAS via *in situ* gas foaming and freeze-drying. We hypothesize that 3DHAS possess enhanced biomechanical properties and bioactivity, which could collaboratively promote cellular infiltration and chondrification both *in vitro* and *in vivo*. Therefore, the composition, microstructure, mechanical properties, and biocompatibility of scaffolds were evaluated. The bioactivity of scaffolds was investigated *in vitro* as well as *in vivo* after subcutaneous implantation in nude mice. Moreover, the potential of scaffolds for the regeneration of articular cartilage *in vivo* was evaluated after implantation in articular cartilage defect model in rabbits (Fig. 1).

2. Experimental

2.1. Materials

Poly(L-lactide-co-ε-caprolactone) (PLCL, Mw = 300 kDa) with an L-lactic acid/ε-caprolactone ratio of 50:50 was supplied by Jinan Daigang Biomaterial Co., Ltd. (Jinan, China). Cocoon was purchased from Jiaxing Silk Co., Ltd. (Jiaxing, China). 1,1,1,3,3,3-hexafluoro-2-propanol (HFIP) was purchased from Shanghai Darui Fine Chemical Co., Ltd. (Shanghai, China). Hyaluronic acid sodium salt (HA, MW = 1.5 × 10⁶ Da) was obtained from Aladdin Chemistry Co., Ltd. (Shanghai, China). Sodium borohydride was purchased from

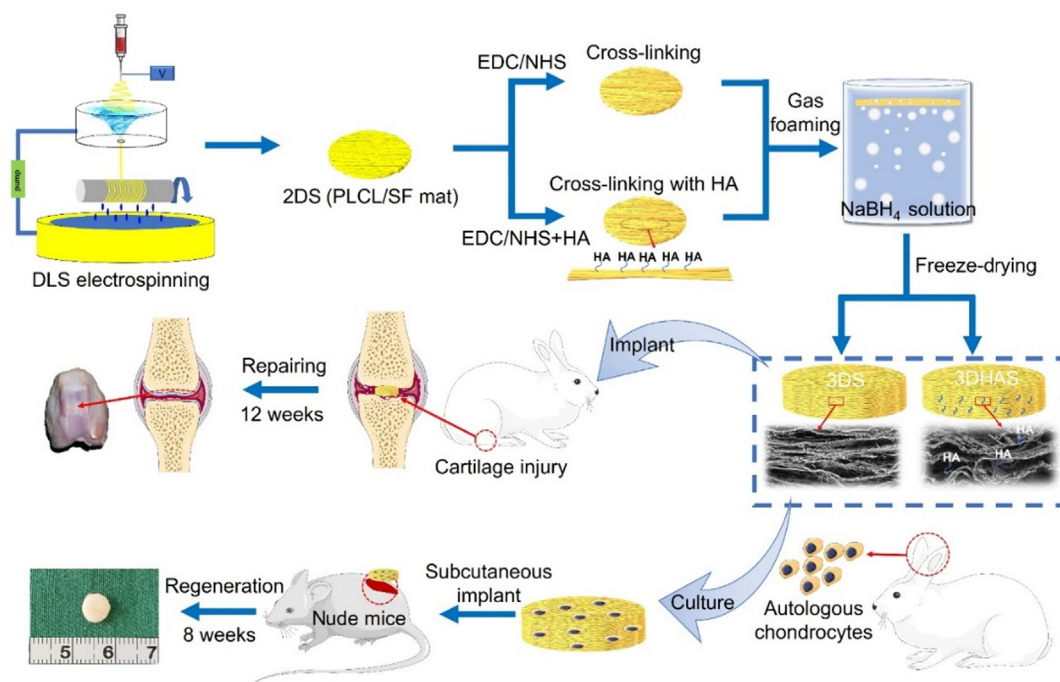


Fig. 1. Schematic illustration of the synthesis of 2DS, 3DS, and 3DHAS scaffolds and their application for cartilage tissue engineering.

Sinopharm Chemical Reagent Co., Ltd. (Shanghai, China). All chemicals were of reagent grade and used as received without any further purification or modification.

2.2. Fabrication of two-dimensional nanofibrous membranes

Two-dimensional PLCL/SF scaffolds (2DS) were fabricated by using a DLS electrospinning system as described previously [27]. Specifically, a water vortex was created in the plastic basin through a central hole (8 mm). The drained water was deposited in the bottom basin and recirculated to the top basin by a pump (2 L/min) to maintain a stable water level. PLCL and SF (8:2, w/w) were dissolved in HFIP at a concentration of 10% (w/v). The solution was transferred into a 10-mL syringe 10 cm above the water vortex and pumped at a flow rate of 1.2 mL/h with 12 kV of an applied voltage. When electrospun nanofibers reached the center of water surface, they flew with the current from the water surface to the vortex. During this time, nanofibers were twisted and organized into nanoyarn by the water vortex. The nanoyarn dropped along the drain hole, which were collected on a mandrel at lower speed (60 rpm). Next, the frozen 2DS were immediately transferred to a lyophilizer for 48 h to obtain dried 2DS.

2.3. Preparation of 3D PLCL/SF scaffolds and HA-crosslinked 3D scaffolds

For the fabrication of three-dimensional PLCL/SF scaffolds (3DS), dried 2DS was first cross-linked with 50 mL solution containing 30 mM 1-ethyl-3-(3-dimethylaminopropyl) carbodiimide (EDC), 8 mM *N*-hydroxysuccinimide (NHS), and 50 mM 2-morpholinoethanesulfonic acid (MES) buffer for 3 h. Scaffolds were washed thrice with deionized water to remove salt and vacuum dried. Afterwards, dried 2DS were immersed into the NaBH₄ solution (0.1 M). The hydrogen bubbles are produced according to equation (1) (Eq. (1)):



The 3DS were removed from the solution at certain time intervals and washed thrice with deionized water. To maintain the integrity of the nanofiber scaffolds, 3DS were freeze-dried by using a lyophilizer.

For preparing HA-crosslinked 3D scaffolds (3DHAS), dried 2DS were cross-linked with 50 mL of MES buffer solution (50 mM) containing 0.5% (w/v) HA, 30 mM EDC, and 8 mM NHS for up to 3 h. The scaffolds were subsequently washed thrice with deionized water to remove free HA and salt, and then vacuum dried. The HA cross-linked 2D mats were further processed for the gas foaming and then freeze-dried to afford 3DHAS.

2.4. Characterization

2.4.1. Morphological analysis

The morphology of different scaffolds was studied by scanning electron microscopy (SEM, Phenom XL, Phenom Scientific Instruments Co. Ltd., Shanghai, China). Samples were sputter-coated with Au by using a carbon tape and subsequently imaged at an accelerating voltage of 10 kV. The pore size and gap distance of scaffolds were measured by using Image J software based on SEM images. The gap distances, lengths of sides in the triangle and rhomboid were measured and recorded in Microsoft Excel, and then the pore area ($n = 20$) was calculated with a formula in Excel.

2.4.2. Fourier transform infrared spectroscopy

Attenuated total reflection Fourier-transform infrared spectroscopy (ATR-FTIR) of samples was recorded by using a Nicolet-670 FTIR spectrometer (Thermo Fisher Scientific, USA). All spectra were recorded in the wavenumber range of 4000–400 cm⁻¹.

2.4.3. Thermogravimetric analysis

Thermal gravimetric analysis (TGA) was performed to evaluate the thermal stability of different samples. Thermograms were recorded with a Libra 209F1 TGA (Selb, Germany) from room

temperature for up to 900 °C, at a heating rate of 20 °C/min under the nitrogen environment (20 mL/min).

2.4.4. Mechanical properties

To analyze the mechanical properties of 3DS and 3DHAS in wet state, rectangular-shaped specimens (10 mm × 10 mm × 3 mm) were used. The measurement of compressive strength was carried out by using a universal testing machine (Instron-5542, Canton, USA) equipped with a 10 N load cell. A total 50 loading–unloading fatigue cycles were performed under a constant displacement rate of 10 mm/min. Compressive moduli of scaffolds were analyzed and calculated by the slope fitting method of the initial linear region of the stress–strain curves.

2.4.5. Water absorption capacity

The water absorption capacity of scaffolds was measured by the following protocol: The sample was weighed (w_d) and submerged into distilled water at ambient temperature for up to 2.5, 5, and 15 min. The excess water was removed by using a filter paper and the sample was weighed again (w_w). The water absorption rate (w) was calculated according to Eq. (2):

$$w = \frac{(w_w - w_d)}{w_d} \times 100\% \quad (2)$$

2.5. In vitro blood compatibility studies

For assessing the blood compatibility, freshly drawn rabbit blood was collected into glass tubes and blended with sodium citrate. The 2DS, 3DS, 3DHAS and medical gauze (control) were first cut into circular shapes (about 6.5 mm in diameter) and placed into culture dishes (6 cm in diameter). Next, about 50 μ L of blood (containing 10% sodium citrate) was poured onto the surface of each sample. The materials were incubated at 37 °C for 5 min. Then, 5 mL of distilled water was added from the edge of culture dishes. Red blood cells that are not trapped within the blood clots will be hemolyzed in water.

To observe the interfacial interactions between the samples and blood cells, a drop of whole blood (containing 10% sodium citrate) was added onto the 2DS, 3DS and 3DHAS. After incubation at 37 °C for 5 min, the samples were rinsed with phosphate buffer solution (PBS) to remove blood cells that were not adhered to the samples. Then, blood cells were fixed with 2.5% glutaraldehyde for 1 h. After dehydration and freeze-drying, the interfacial interaction was observed by SEM.

To measure the blood absorption capacity, the 2DS, 3DS, 3DHAS, and medical gauze (control) were soaked in whole blood for 5 min at 37 °C. The blood absorption was calculated according to Eq. (3):

$$\text{Blood absorption}(\%) = \frac{(M_1 - M_0)}{M_0} \times 100 \quad (3)$$

where M_0 is the weight of dry 2DS, 3DS and 3DHAS, or dry medical gauze, and M_1 is the weight of each material after absorbing whole blood.

To measure the blood clotting time, 10 mg of each sample was added into tubes and then 2 mL of the whole blood (containing 10% sodium citrate) was added to each tube; medical gauze was used as a control. Then, 60 μ L of CaCl_2 (0.25 mol/L) solution was added into the tube. The tube was tilted every 15 s, and the time at which the blood stopped to flow was recorded.

The erythrocytes (Shanghai Jiagan Biotechnology Co., Ltd., China) were washed thrice with PBS and centrifuged at 3000 rpm for 10 min at room temperature, and then diluted to 10 v/v% with PBS buffer. The diluted erythrocytes solution (200 μ L) and the PBS buffer (800 μ L) were added into a 1.5 mL tube, which contained the 2DS, 3DS and 3DHAS. All tubes were incubated under gentle

agitation for 60 min at 37 °C, and then centrifuged at 2000 rpm for 5 min at room temperature. The absorbance of the supernatant was measured at 540 nm by using a microplate reader. The erythrocytes in PBS buffer were used as a negative control, and the erythrocytes lysed with pure water were as a positive control. The hemolysis percentage (HP) was calculated by the following Eq. (4):

$$\text{HP}(\%) = \left[\frac{(A_t - A_{nc})}{A_{pc} - A_{nc}} \right] \times 100\% \quad (4)$$

where A_t is the absorbance of tested samples; A_{nc} and A_{pc} are the absorbance of the negative and positive control, respectively.

2.6. Cell culture studies in vitro

For the *in vitro* cell culture experiments, chondrocytes were isolated from the auricular cartilage of New Zealand white rabbits and cultured in Dulbecco's modified Eagle's medium (Gibco, USA) containing 10% fetal bovine serum at 37 °C as previously described [28]. Chondrocytes of the passage 2 were used for the *in vitro* studies.

For cell adhesion and proliferation assays, 2DS, 3DS and 3DHAS scaffolds (disk-shaped samples of 10 mm diameter and 0.8 mm thickness for 2DS, and 10 mm diameter and 3 mm thickness for both 3DS and 3DHAS) were sterilized by UV for 2 h. The cell adhesion and proliferation of chondrocytes on the scaffolds was determined by seeding the scaffolds with the chondrocytes in 48-well plates as described previously. Briefly, chondrocytes were evenly seeded onto scaffolds at a density of 3.0×10^4 cells/well. After an initial incubation of the cell-seeded scaffolds for 4 h, the medium containing unadhered cells was collected from different groups, and the cell numbers were counted (lost cell number). The cell adhesion rate of the samples was calculated according to Eq. (5):

$$\text{Cell adhesion rate}(\%) = \frac{\text{Total numbers of cell} - \text{Number of the lost cells}}{\text{Total numbers of cells}} \times 100\% \quad (5)$$

The cell proliferation at day 1, 3, and 7 was examined by using a cell counting kit 8 (CCK-8) assay. Briefly, chondrocytes were seeded on scaffolds with a density of 3.0×10^4 cells/well and the medium was removed at day 1, 3, and 7. The scaffolds were washed thrice with PBS and then incubated with the 200 μ L of the fresh medium containing 20 μ L of CCK-8 and 180 μ L of serum-free medium per well. After an incubation for 2 h at 37 °C, 100 μ L of the medium was transferred into a 96-well plate to measure the optical density (OD) at a wavelength of 450 nm, and the mean value derived from four wells was calculated.

In addition, the viability of seeded cells was determined by using a Live/Dead cell assay kit (In vitrogen, USA) at day 3. The fluorescence images of the samples were obtained by using a confocal laser scanning microscope (Nikon, A1RMP, Japan).

The cell cytoskeleton was stained by using F-actin and phalloidin and the nuclei were stained with 4',6-diamidino-2-phenylindole (DAPI). Chondrocytes (3.0×10^4 cells mL^{-1}) were seeded on 2DS, 3DS and 3DHAS for up to 3 days. After the removal of the medium, cells were washed with PBS thrice and fixed with 4% paraformaldehyde (PFA) at room temperature for up to 30 min. Afterwards, the scaffolds were washed with PBS thrice and immersed in a permeabilization and blocking buffer (1% bovine serum albumin and 0.1% triton in PBS) for 30 min. Next, the chondrocyte-seeded scaffolds were washed with PBS and stained with an appropriate dilution of phalloidin in the dark for 30 min, followed by washing with PBS thrice and stained with DAPI for the nuclei. The cell cytoskeleton was measured by using a confocal laser scanning microscope (Nikon, A1RMP, Japan).

The samples were chemically fixed to examine the cell attachment by SEM. Briefly, chondrocytes (3.0×10^4 cells mL^{-1}) were cultured on 2DS, 3DS and 3DHAS. At pre-determined time points, the medium was removed and the cell-seeded scaffolds were washed thrice with PBS. Scaffolds were immersed into PFA for 2 h, washed with PBS thrice, and dehydrated in a gradient series of ethanol (30–100%) for 15 min each. After drying in the fume hood, the morphology of cells was observed by using SEM.

Cell infiltration was evaluated by hematoxylin and eosin (H&E) staining. Chondrocyte (3.0×10^4 cells mL^{-1}) were seeded on 2DS, 3DS and 3DHAS. At pre-determined time points, cells were fixed with PFA for 1 h and scaffolds were dehydrated through a series of ethanol as previously described. After embedding in the paraffin, the scaffolds were sectioned (5 μm) and stained by using H&E. Finally, the infiltration of cells into the scaffolds was observed by an optical microscope (Leica Microsystems, Germany).

Immunofluorescence staining for the collagen types II was performed on sectioned slices of cell-seeded samples. Chondrocytes (3.0×10^4 cells mL^{-1}) were seeded on 2DS, 3DS and 3DHAS for up to 2 weeks. After embedding in the paraffin, the scaffolds were sectioned (5 μm) and deparaffinized. Deparaffinized sections were permeabilized in 0.1% (v/v) Triton-X (Sigma), and blocked with 10% (v/v) normal goat serum for 45 min. Sections were incubated with anti-collagen II antibody (ab34712, Abcam; 1:100 dilution) at 4 °C for overnight. After washing thrice with 0.1% bovine serum albumin (BSA)/PBS, sections were incubated with fluorescent-labeled secondary antibodies (Alexa-Fluor 546; Life Technologies). The nuclei were stained with DAPI for 5 min at room temperature. Imaging was carried out using a fluorescence microscope (Leica Microsystems, Germany).

Expression of cartilage-related genes (collagen type II (COL II), sex determining region Y box 9 (SOX 9), aggrecan (ACAN), hypertrophic gene (collagen type X (COL X)), and fibroblastic phenotype gene (collagen type I (COL I)) was analyzed by Real-time PCR (RT-PCR). Cell-laden scaffolds ($n = 3$) were collected on week 2 and ground within TRIzol reagent (Invitrogen) to extract total mRNA. 1 μg of RNA was used for cDNA synthesis by M-MLV cDNA Synthesis Kit (Promega) according to the manufacturer's instruction. RT-PCR was performed using SYBR Green PCR Master Mix (Enzyomics) and ABI StepOnePlus™ Real-Time PCR system (Applied Biosystems). All primer sequences are listed in Table S1 (supplementary information). The expression of all genes was normalized to the housekeeping gene glyceraldehyde 3-phosphate dehydrogenase (GAPDH) and to gene expression of chondrocytes before seeding into the different samples at day 0 and the relative expression was calculated by $-2^{\Delta\Delta\text{Ct}}$ method.

2.7. In vivo animal studies

2.7.1. Cartilage regeneration in nude mice

All animals (nude mice and rabbit) were obtained from Shanghai Jiao Tong University (SJTU) and treated according to the standard guidelines approved by the ethics committee of SJTU. The chondrocytes (passage 2) were harvested from auricular cartilage of New Zealand white rabbits as described above and seeded onto scaffolds to form cell – scaffold constructs. Briefly, 200 μL suspension of chondrocytes with a concentration of 5.0×10^8 cells/mL were evenly seeded onto 3DS and 3DHAS (diameter, 6.5 mm and thickness, 2.5 mm). These cell-scaffold constructs were incubated for 4 h without medium at 37 °C and then further cultured in DMEM for up to one week *in vitro*. Nude mice were anesthetized with 4% isoflurane and the skin was disinfected with a povidone-iodine solution. After that, an incision of 1.5 cm was made on the back of each mouse, the cell-scaffold constructs were implanted into the subcutaneous pocket of the nude mice ($n = 3$ per group) for up to eight weeks. Cell-scaffold constructs along with the

surrounding tissues were retrieved and fixed in 4% PFA for up to 3 d for H&E and Safranin-O staining. To evaluate the cartilage-specific phenotypes, collagen type II was detected by immunohistochemical staining.

2.7.2. Biochemical and biomechanical analyzes of regenerated cartilage

The content of cartilage-specific matrices in cell-scaffold constructs was analyzed quantitatively. Cartilage samples for biochemical analyzes were digested in proteinase K (1 mg/mL in 50 mM Tris with 1 mM ethylene diamine tetra-acetic acid (EDTA), 1 mM iodoacetamide, and 10 mg/mL pepstatin A; all from Sigma-Aldrich) for 16 h at 56 °C. DNA content was determined by using a total DNA quantification assay (PicoGreen dsDNA assay, Invitrogen, United States) in accordance with the manufacturer's instructions.

Total glycosaminoglycans (GAGs) content were analyzed by spectrophotometric microdetermination with dimethylmethylene blue [29]. Briefly, total GAGs were precipitated by guanidinium chloride solution (0.98 mol/L). After dissolving the GAGs precipitate, the OD values were determined at 595 nm. A standard curve was established using chondroitin-4-sulfate, and total GAGs were determined from the OD value correlating to the corresponding GAGs amount in the standard curve.

The total collagen content was measured by using a hydroxyproline assay. Samples were prepared by alkaline hydrolysis, and free hydroxyproline hydrolyzates were assayed according to previously described methods [30]. The hydroxyproline content was finally converted to total collagen content according to the mass ratio of collagen to hydroxyproline of 7.25.

The compressive moduli of the cell-scaffold constructs and native tissue were determined by using a biomechanical analyzer (Instron-5542, Canton, USA) as described previously [28]. Samples were subjected to a continuous planar unconfined strain rate of 1 mm/min until 50% of deformation. The compressive moduli of scaffolds were calculated based on the slope of the stress-strain curve.

2.7.3. In situ articular cartilage regeneration in rabbits

Adult male New Zealand white rabbits, 4 months old and weighing approximately 2.5–3.0 kg were used to evaluate the potential of scaffolds for the regeneration of articular cartilage and divided into three groups ($n = 4$ for each group), namely, the non-treated group, 2DS group, 3DS group, and 3DHAS group. Both knees of each rabbit were used for the implantation of scaffolds and defects were left untreated in the non-treated group. The rabbits were anesthetized with 10% chloral hydrate (4 mL/kg) and the knee joint of the rabbits was exposed after dislocating the patella. The full-thickness cartilage defects (4 mm in diameter, 3 mm in depth) was created by using a stainless-steel punch on the trochlear groove of the distal femur and implanted with the 2DS (4 mm in diameter, 1 mm in thickness) and matching 3DS as well as 3DHAS (4 mm in diameter, 3 mm in thickness). Finally, the operated knee joints were closed with sutures (4-0 thread), and antibiotics were administrated intramuscularly for prophylactic infection. Rabbits were sacrificed at 12th weeks after surgery.

2.7.4. Histology and immunohistochemistry staining

The histological specimens of rabbit articular cartilage were harvested, fixed, decalcified, paraffin-embedded, and sectioned. The histological sections (5 μm thick) were stained for H&E, Safranin-O and fast green (Saf-O/FG). The immunohistochemical staining was performed for the collagen type I and II. For H&E staining, tissue sections were stained with Harris hematoxylin solution for 10 min, followed by counterstaining with eosin-phloxine solution. For Saf-O/FG staining, tissue sections were

stained in fast green (0.05%, w/v) for 5 min, followed by staining in safranin O (0.1%, w/v) solution for 5 min. For the immunohistochemical staining, tissue sections were incubated with hydrogen peroxide to block endogenous peroxidase, followed by heat treatment at 60 °C for 1 h to retrieve antigen. Monoclonal antibodies against collagen type I (ab34710, Abcam), and collagen type II (ab34712, Abcam) were then added onto scaffolds and they were incubated overnight at 4 °C, followed by addition of a biotinylated IgG antibody. After incubation with streptavidin peroxidase, the sections were stained with 3, 3'-diaminobenzidine as the chromogenic agent. International Cartilage Repair Society (ICRS) macroscopic scoring (shown in Table S2 of the Supporting Information) and Modified O'Driscoll histological scoring (shown in Table S3 of the Supporting Information) was adopted to reveal the integration with the original cartilage and the secretion of cartilage matrix. The gross photographs and histological staining images were observed and evaluated by three individuals.

2.8. Statistical analysis

All of the data were obtained in triplicate, and the values were expressed as mean \pm standard deviation (SD). For statistical significance, Student's *t* test or one-way analysis of variance (ANOVA) with Tukey's post-hoc test was performed where appropriate. The significant data were marked by using an asterisk (*) and the criterion for statistical significance was **p* < 0.05.

3. Results

3.1. Preparation and characterization of 2DS, 3DS and 3DHAS

The schematic diagram of the fabrication of 2DS, 3DS, and 3DHAS scaffold is illustrated in Fig. 1. The fabrication process can be divided into four steps: (1) DLS electrospinning, (2) cross-

linking, (3) gas foaming, and (4) freeze-drying. Given to the ease of the fabrication of scaffolds, the mass production of scaffolds is envisioned.

As shown in Fig. 2, electrospun nanofiber mats were successfully expanded into 3D scaffolds after treatment with the NaBH₄ solutions and freeze-drying. Fig. 2A shows the schematic of the direction of alignment of scaffolds; the red arrow represents the direction of the alignment of the nanofibers and yarns. Fig. 2B showed photographs of a relatively uniform 2DS (10 mm \times 10 mm) with an approximate thickness of 1 mm. The 3D scaffolds displayed different values of the thickness after foaming for up to different time points. As shown in Fig. 2C–F, the thickness of the gas foamed nanofiber scaffolds increased with the foaming time. After treatment with NaBH₄ solution only for up to 5 min, the thickness of 3D scaffold was increased from 1 mm to 3 mm, which further increased to 4 mm after 20 min of the foaming treatment (Fig. 2G). This shows that the thickness of the scaffolds could be tailored by controlling the processing time. Similarly, the porosity of the 3D scaffolds increased from 72% for the raw 2DS to 88% and 94% after 5 min and 20 min of the foaming treatment, respectively (Fig. 2H). The density of the 2DS was found to be 0.2 g/cm³, which decreased to 0.08 g/cm³ and 0.05 g/cm³ after foaming for up to 5 and 20 min, respectively (Fig. 2I). On the other hand, 3DS and 3DHAS scaffolds did not show an appreciable difference in the thickness, porosity, and density with an increase in the foaming time. After 5 and 20 min of gas foaming, 3DHAS exhibited a regular cubic shape and a distinct outline, which were better than that of the uneven thickness and the local bulging of the 3DS scaffolds. It may be attributed to the different degree of cross-linking inside 3DS, which may lead to different responses to the pressure exerted by the air bubbles within the scaffold. However, the introduction of HA may further consolidate the scaffold in weaker crosslinking regions, which may result into a better morphological retention. 3DS and 3DHAS exhibited similar water absorption behavior

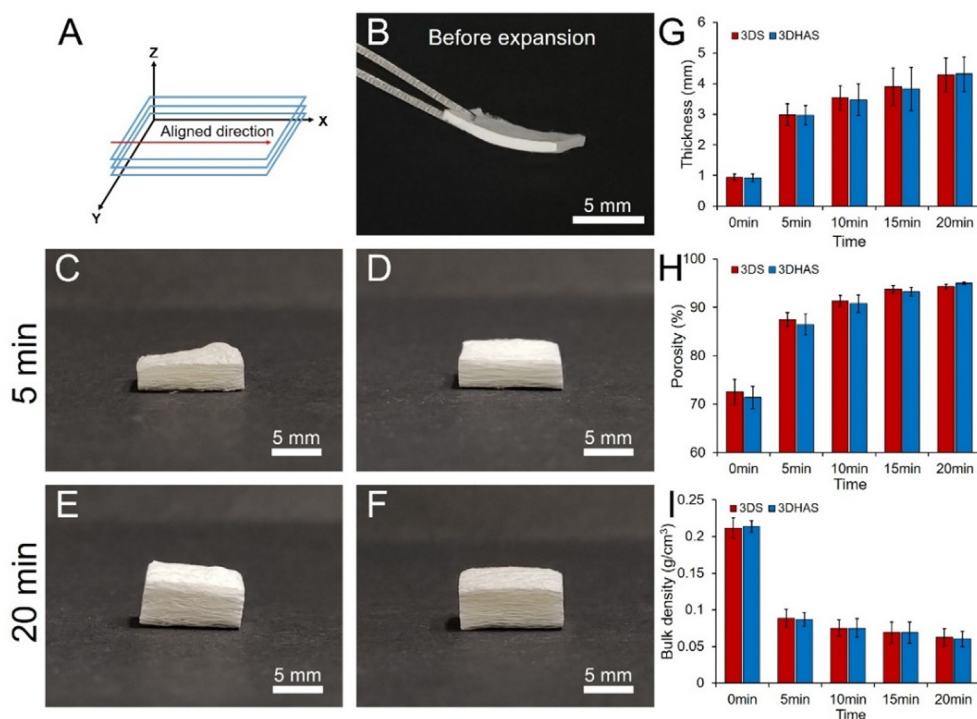


Fig. 2. Expansion and characterization of 2DS, 3DS and 3DHAS. (A) The schematic shows the alignment direction of the scaffolds. (B) Photographs of 2DS (raw nanofiber mat), 3DS (C), and 3DHAS (D) after an expansion into the foaming agent for up to 5 min. Photographs of 3DS (E) and 3DHAS (F) after an expansion into foaming agent for up to 20 min. (G) Thickness of the 3DS and 3DHAS treated with 0.1 M NaBH₄ solution for different time points. (H) Porosity of the 3DS and 3DHAS treated with 0.1 M NaBH₄ solution for different time points. (I) Bulk density of the 3DS and 3DHAS treated with 0.1 M NaBH₄ solution for up to different time points.

(Fig. S1); both types of scaffolds attained equilibrium water adsorption capacity and achieved the maximum water absorption rate ($\approx 1500\%$) in less than 5 min, which was significantly higher than that of the 2DS ($\approx 500\%$). These results indicate that the water could be absorbed into the 3D scaffolds readily as compared to their 2D counterparts. The high porosity and multi-layered structure of the 3D scaffolds lead to the higher water absorption, which may be beneficial for the cartilage regeneration.

To reveal the detailed morphological structure of 2DS, 3DS, and 3DHAS scaffolds, SEM analysis was carried out. Prior to the expansion, the cross-section of 2DS was mainly composed of an aligned fibrous structure (Fig. 3A and B). The dense surface of 2DS consisted of compact aligned nanofibers and yarns (Fig. 3C). After treatment with the NaBH_4 solution, the 3DS scaffolds with a continuous layered structure were successfully obtained, which also exhibited laminated fibrous layers (Fig. 3D and E). The distance among the layers in the 3DS was larger than that of the 2DS, and a loose surface interlaced with aligned yarns and nanofibers was formed (Fig. 3F). In contrast, 3DHAS did not only exhibit a highly continuous layered structure with preserved nanotopographical cues, but also a honeycomb-like nanofiber network of HA (Fig. 3G-L).

The distribution of the gap distance for the cross-sections of 2DS, 3DS and 3DHAS was also quantified. Most of gap distances were around 2–8 μm prior to gas foaming (Fig. 3M). After expansion, the gap distances corresponding to the peaks were increased to approximately 20 and 60 μm within the cross-sections of 3DS for x-z and y-z direction, respectively (Fig. 3N). 3DHAS also showed an increase in the gap distances corresponding to the peaks, which were found to be 30 and 50 μm for x-z and y-z directions, respectively (Fig. 3O). In addition, the surface pore area of 3DS and 3DHAS was $129 \pm 67 \mu\text{m}^2$ and $125 \pm 47 \mu\text{m}^2$, which was significantly higher than that of 2DS ($10 \pm 6 \mu\text{m}^2$) (Fig. 3P). SEM images showed that 3D scaffolds exhibited a layered structure and a porous architecture, which would be beneficial for the exchange of the nutrients and cell-cell communication.

FTIR analysis was carried out to investigate the composition of scaffolds and the spectra were displayed in Fig. 4A-B. The HA showed a broad absorption band at approximately 3310 cm^{-1} , which is attributed to the O–H and N–H stretching vibrations. The bands appeared at 1610 cm^{-1} and 1401 cm^{-1} are ascribed to the carbonyl stretching vibration of the carboxylate group [31]. Typical peaks of C–O stretching vibrations were observed at 1020 cm^{-1} and 1080 cm^{-1} , while the shoulder at 1152 cm^{-1} corre-

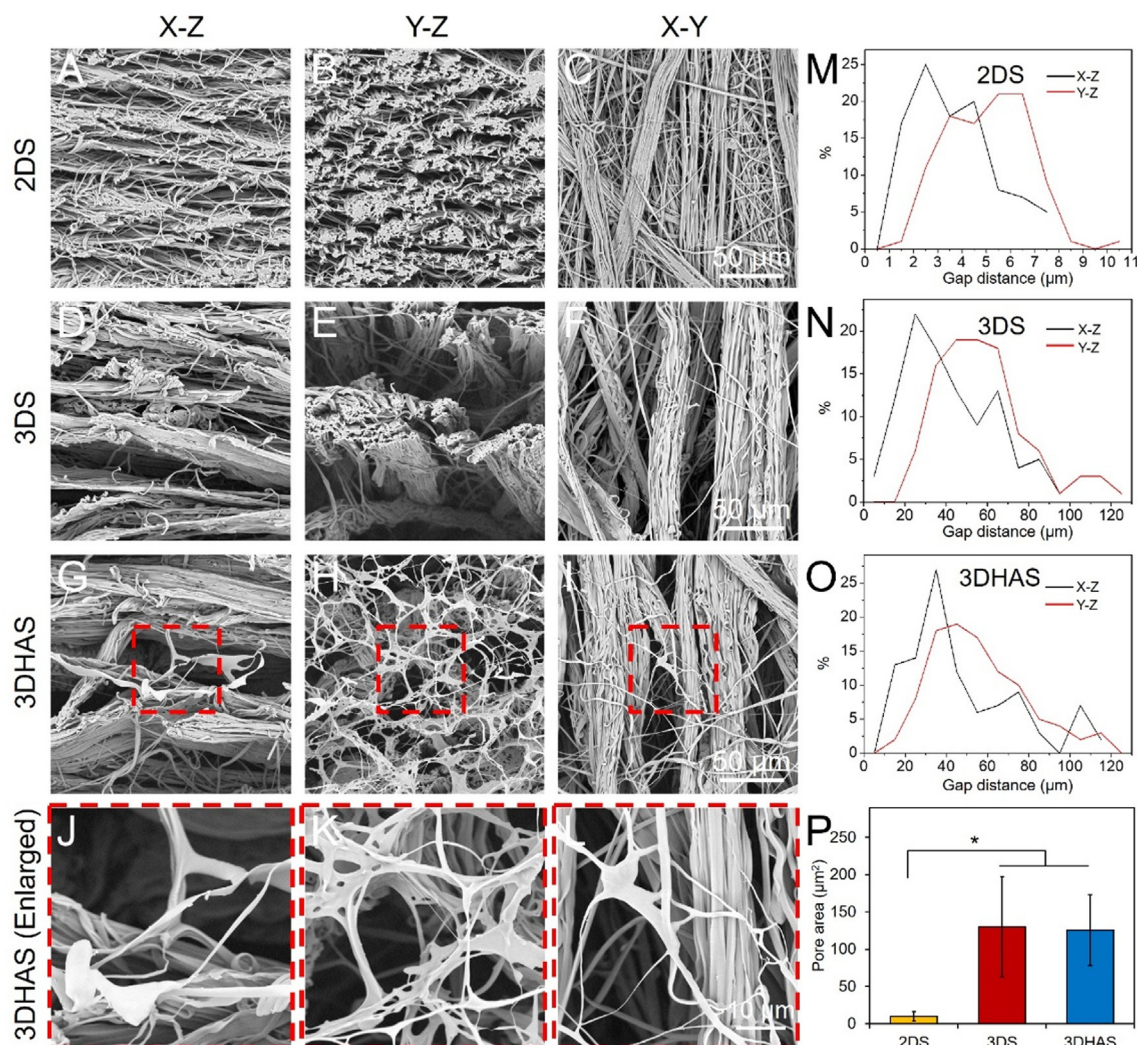


Fig. 3. Morphological and structural characterizations of 2DS, 3DS and 3DHAS. SEM micrographs of 2DS (A–C), 3DS (D–F), and 3DHAS (G–L) in different directions before and after expansion. The distributions of gap distances between adjacent layers of 2DS (M), 3DS (N), and 3DHAS (O) in different directions. (P) Pore area of 2DS, 3DS, and 3DHAS, * $p < 0.05$.

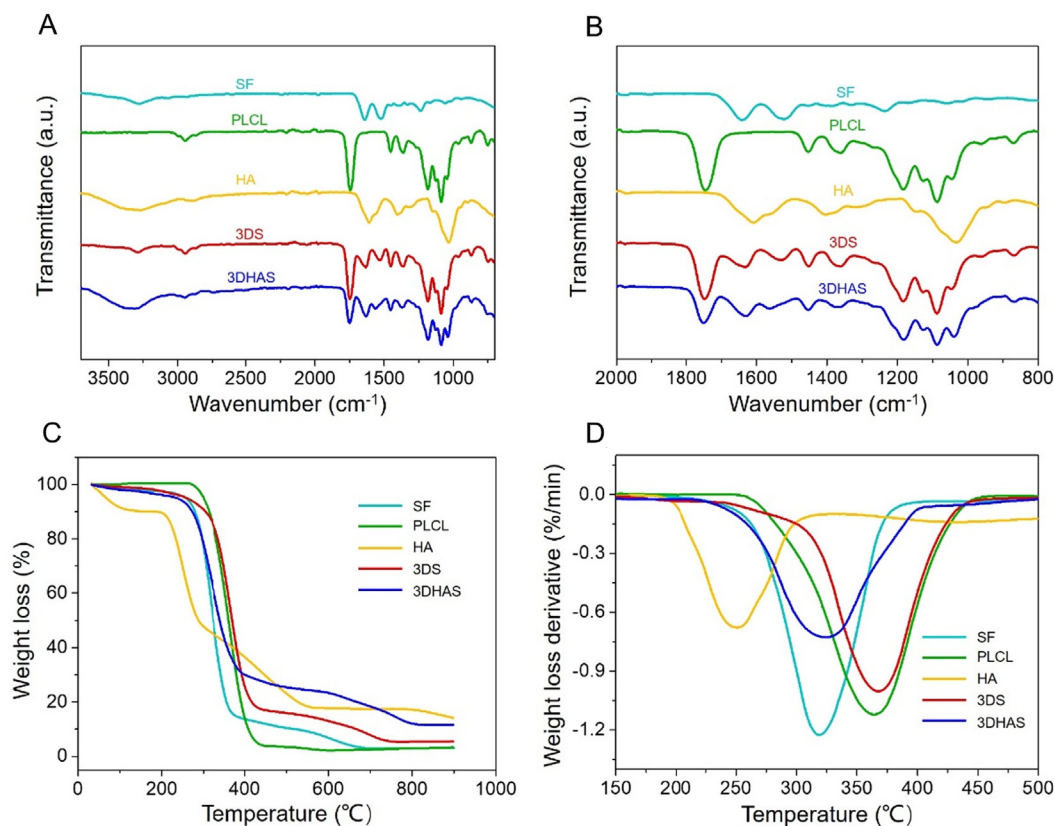


Fig. 4. ATR-FTIR spectra of the SF, PLCL, HA, 3DS, and 3DHAS. (A) Spectra in the range of 3800 cm^{-1} to 800 cm^{-1} and (B) 2000 cm^{-1} to 800 cm^{-1} . (C) TG curves and (D) DTC curves of SF, PLCL, HA, 3DS, and 3DHAS.

sponded to the C–O–C stretching vibrations in glycosidic groups [32].

In the spectrum of 3DS, a peak at 3295 cm^{-1} corresponding to the stretching vibration of N–H of the SF was observed. Additionally, the peaks at 1639 cm^{-1} and 1520 cm^{-1} corresponded to amide I and amide II bonds, respectively. It was indicated that after the cross-linking and foaming treatment, SF mainly exhibited β -sheet structure in the 3DS. Before gas foaming, 2DS were cross-linked by using EDC/NHS, which may cause conformational transformation in the SF due to the formation of an amide bond between the amino and carboxyl groups within the SF. Moreover, during the subsequent freeze-drying process, volatiles from the other samples containing insoluble organic solvents may come into contact with the SF and result into a conformational change of SF from the random coil-like structure to the β -sheet like structure [33]. The PLCL spectrum exhibited a typical absorption band at 2938 cm^{-1} , which was ascribed to the $-\text{CH}_2-$ stretching vibration. The band appeared at 1756 cm^{-1} could be assigned to the stretching vibration of the carbonyl groups of esters. The characteristic peaks located at 1454 cm^{-1} and 1359 cm^{-1} can be attributed to the C–H symmetric and asymmetric vibrations of PLCL, respectively. 3DS scaffolds displayed all of the aforementioned characteristic peaks of SF and PLCL, indicating that no chemical reaction occurred during the foaming process.

3DHAS also displayed the characteristic bands of both the PLCL and SF. In addition, a broad band appeared at 3310 cm^{-1} was assigned to the O–H stretching vibrations from the HA. The EDC/NHS reagent enabled the formation of amide bonds between the carboxylic groups and the amine groups of HA and SF [26]. The amide bond II was shifted from 1520 cm^{-1} toward 1553 cm^{-1} , which confirmed the crosslinking between HA and SF [31,34].

Additionally, the intensity of the carboxylate bands at 1610 cm^{-1} and 1401 cm^{-1} was reduced, which indicated that some of the carboxylic groups have been consumed, while some of them still remained non-crosslinked.

TGA curves of different samples were displayed in Fig. 4C. For pure PLCL, the thermal degradation temperature varied between $270\text{ }^\circ\text{C}$ and $425\text{ }^\circ\text{C}$, while no obvious mass change occurred below $100\text{ }^\circ\text{C}$, which was attributed to the hydrophobic nature of scaffolds. The residual mass was found to be 3 wt% at $900\text{ }^\circ\text{C}$, which showed that the PLCL was almost fully decomposed. On the other hand, the TGA curves of HA, SF, 3DS and 3DHAS exhibited 8.85%, 1.70%, 0.93%, and 1.93% mass loss, respectively below $100\text{ }^\circ\text{C}$, which was ascribed to the removal of the physically absorbed water from the fibers or the residual solvent components. The main degradation of SF occurred in the range of $215\text{--}405\text{ }^\circ\text{C}$, which was attributed to the cleavage of the peptide bonds of SF and the residue was about 3.22 wt% at $900\text{ }^\circ\text{C}$. The main weight loss of pristine HA occurred in the range of $195\text{--}570\text{ }^\circ\text{C}$, which was ascribed to the breakdown of the main polysaccharide chain of HA and the residual mass of HA was around 14.19 wt% at $900\text{ }^\circ\text{C}$, indicating a high yield of the residual pyrolyzed carbonaceous materials. For 3DS, the main thermal degradation temperature range was in the range of $215\text{--}425\text{ }^\circ\text{C}$ corresponding to the onset decomposition temperature of SF and the final decomposition temperature of PLCL. The residual mass of 3DS was found to be 5.47 wt% at $900\text{ }^\circ\text{C}$. On the other hand, 3DHAS displayed higher thermal stability than that of the HA and SF; the degradation temperature shifted toward the higher temperature region ($225\text{--}800\text{ }^\circ\text{C}$), which may be ascribed to the hydrogen bonding between the hydroxyl groups of HA and the formation of amide bonds with the SF. 3DHAS also exhibited a higher residue (11.59 wt%) as compared to 3DS

(5.47 wt%), indicating the presence of the hyaluronic acid component in 3DHAS after cross-linking and foaming treatment, thus leading to a higher pyrolyzed carbon residue.

The maximum degradation temperature (T_{max}) of scaffolds was measured from the DTG curves and displayed in Fig. 4D. The T_{max} was found to be 248 °C, 318 °C, 365 °C, 368 °C and 322 °C in HA, SF, PLCL, 3DS and 3DHAS, respectively. It was found that PLCL conferred good thermal stability to 3DS and 3DHAS scaffolds. Moreover, 3DHAS exhibited higher T_{max} and a broader range of the decomposition temperature than that of the SF, which was plausibly due to the hydrogen bonding and the formation of amide bonds between the HA and the SF. Consequently, the HA-crosslinked 3DHAS were successfully obtained.

3.2. Mechanical properties

Compression tests were conducted to evaluate the mechanical properties of 3DS and 3DHAS. After cross-linking, gas foaming, and freeze-drying, 3DS achieved a stable structure, which can be restored after different degrees of compression (Fig. S2 and Video S1). Fig. 5A showed the representative compressive stress–strain curves of the 3DS and 3DHAS with $\varepsilon = 80\%$. The compressive modulus was found to be 1.37 ± 0.35 kPa and 2.92 ± 0.39 kPa for 3DS and 3DHAS, respectively (Fig. 5B). Quantitative indices of compressive modulus of 3DHAS were significantly increased after cross-linking with the HA. Moreover, the loading–unloading cycle test demonstrated that the 3DHAS groups exhibited higher mechanical properties as compared to the 3DS groups. In addition, both 3DS and 3DHAS exhibited non-linear closed compressive stress–strain curves, indicating low energy of dissipation (Fig. 5C–D). The 3DHAS displayed a higher stress value (3.11 kPa) along with a minimum stress loss (10.45%) after 50 cycles of compression at 50% strain.

3.3. In vitro blood compatibility studies

To evaluate the hemostatic ability of different samples, a blood coagulation test was performed. As shown in Fig. 6A–C, after rinsing the samples, the water around medical gauze and 2DS group turned into red color due to the existence of uncoagulated blood. In contrast, only a slight red color was observed around 3DS, which was almost transparent around 3DHAS. These results indicated that it was difficult for the blood to coagulate on the medical gauze and 2DS, which resulted into the dissolution of a large amount of blood in the water after rinsing. On the other hand, multi-layered 3DS and 3DHAS promoted the blood coagulation effect.

The interfacial interaction between different scaffolds and blood cells was discerned by the SEM and shown in Fig. 6D–F. The blood cells were simply attached to the 2DS. On the other hand, blood cells attached onto the surface of the fibers as well as trapped within the nanofibers in 3DS and 3DHAS scaffolds due to the presence of a layered structure.

Additionally, as shown in Fig. 6G, the blood absorption capacity of the 3D scaffolds was higher ($\approx 1700\%$) than that of the 2DS scaffolds ($\approx 800\%$) and medical gauze ($\approx 800\%$). The blood clotting time was also measured and shown in Fig. 6H. 3DS and 3DHAS showed the blood clotting time of 165 ± 15 s and 150 ± 15 s, respectively, which was shorter than that of the 2DS (220 ± 22 s) and medical gauze (240 ± 15 s). Fig. 6I showed the hemolysis ratios of medical gauze and different nanofiber scaffolds. All samples demonstrated hemolysis ratio well-below the international standard (5%) [35] indicating the good blood compatibility of the developed scaffolds.

3.4. In vitro cytocompatibility studies

The results of the Live & Dead cell assay indicated that all of the scaffolds showed minimal cell toxicity at day 3. The chondrocytes

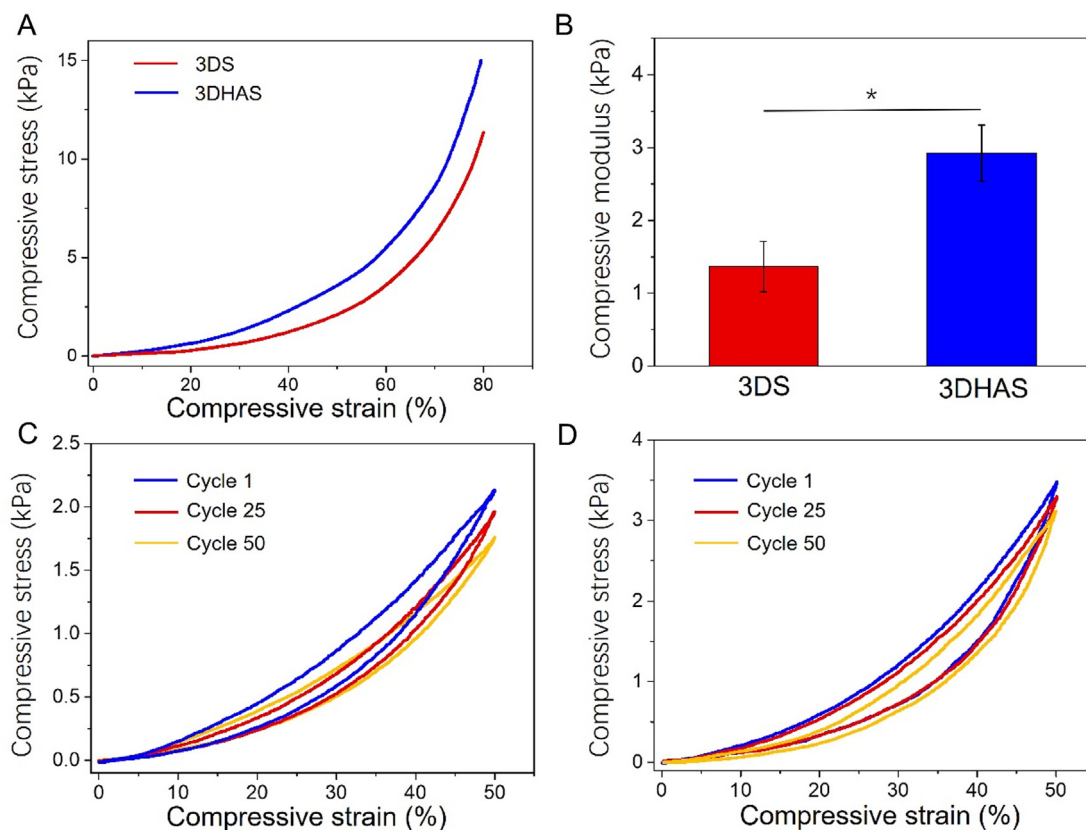


Fig. 5. Compressive mechanical properties of 3DS and 3DHAS. (A) Representative curves of the compression test of 3DS and 3DHAS with $\varepsilon = 80\%$. (B) The statistical analysis of the compressive modulus. Cyclic compressive fatigue test of 3DS (C) and 3DHAS (D) with $\varepsilon = 50\%$. (* $p < 0.05$, $n = 3$).

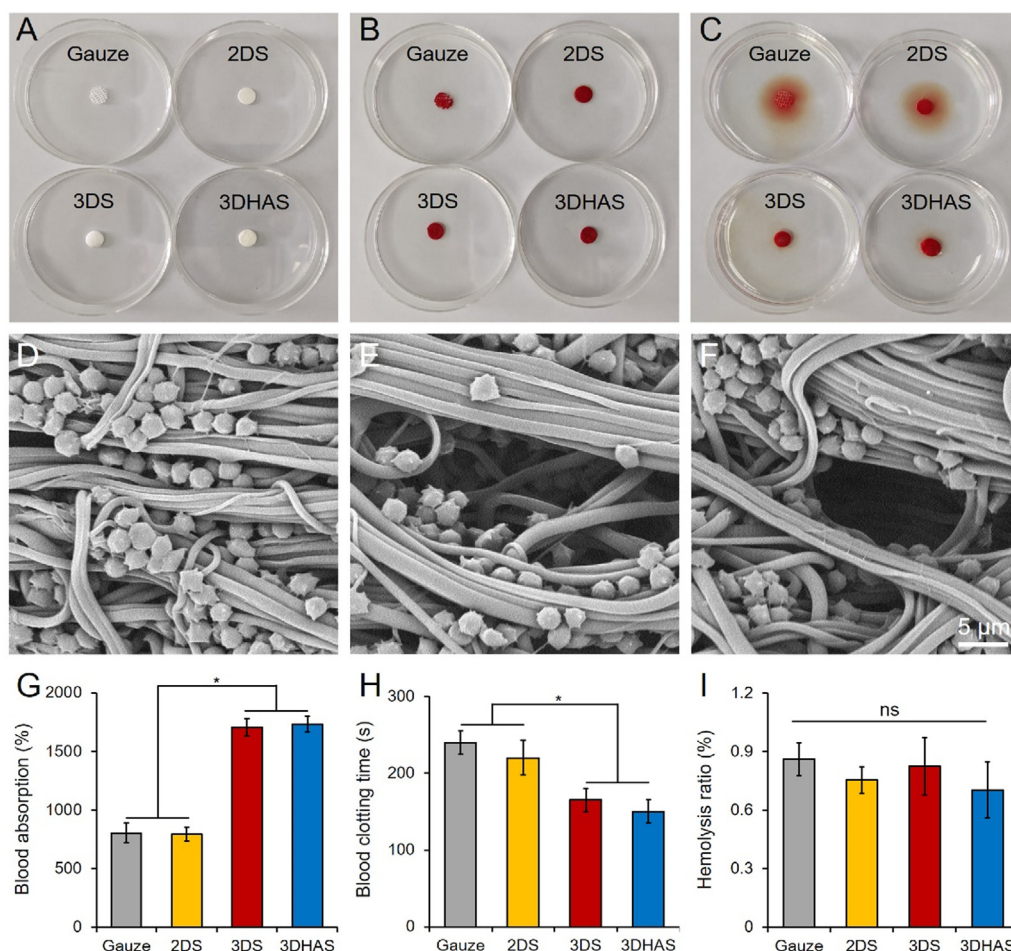


Fig. 6. *In vitro* blood compatibility studies. The photographs of the blood-clotting process: materials used for the blood clotting (A), addition of the 50 μ L of the blood (B), and rinsing by the 5 mL of water (C). SEM images of the interfacial interaction between the blood cells with 2DS (D), 3DS (E), and 3DHAS (F). (G) Blood absorption capacity of medical gauze, 2DS, 3DS and 3DHAS. (H) Blood clotting time in of medical gauze, 2DS, 3DS and 3DHAS. (I) Hemolysis ratio of medical gauze, 2DS, 3DS and 3DHAS. (* $p < 0.05$, $n = 3$).

survived well (green) on the scaffolds and virtually no dead cells (red) could be observed in all three groups at day 3 (Fig. 7A–C). Notably, the numbers of cells in the 3DHAS group were comparable to that in the 3DS. Similarly, 3D scaffolds showed significantly higher numbers of cells than that of the 2DS groups. To examine the effect of the morphology of scaffolds on cell cytoskeleton, immunofluorescence staining for F-actin was performed. Cells cultured on the 3D scaffolds (Fig. 7E–F), especially on 3DHAS (Fig. 7F) showed better cell anchorage as compared to the cells cultured on the 2DS (Fig. 7D), indicating stronger cell-scaffold interactions. The interaction between the cells and the scaffolds on day 7 was further observed by SEM (Fig. 7G–I). Cells localized on the scaffold surface and proliferated along the nanofibers, almost contacting each other and forming cell sheets. As compared to the 2DS, 3D scaffolds exhibit larger pores distribution, which may contribute to the cell infiltration. Besides, 3DHAS showed more population of cells infiltrated within the scaffold, which implies that cells infiltrated more easily within 3DHAS than that of the other groups (Fig. 7J–L).

The initial cell attachment was evaluated after cell seeding for up to 4 h and the results are shown in Fig. 7M. 3D scaffolds displayed significantly higher cell adhesion rate than that of the 2DS which may be attributed to the high surface area and large void size. Cell proliferation was also increased with the passage of time over a period of 7-day (Fig. 7N), implying that cells were able to proliferate on all materials. The 3D scaffolds also showed more cell proliferation than that of the 2DS. Notably, the 3DHAS showed significantly higher cell population than that of the 2DS

and 3DS at day 7, which confirmed that the 3DHAS were more suitable for the growth of chondrocytes. These data indicate that 3DHAS provide a favorable microenvironment for the adhesion, proliferation, and infiltration of chondrocytes *in vitro*.

Immunofluorescence staining for the collagen type II showed that cell-seeded 3DHAS possessed the highest secretion of the collagen type II than that of the 2DS and 3DS scaffolds (Fig. 7O–Q). Real-time PCR was performed to compare the level of the secretion of the chondrogenic genes, such as COL II, SOX9 and ACAN, hypertrophic gene (COL X), and fibroblastic phenotype gene (COL I) at day 14. The data is shown in Fig. 7R–V. 3DHAS significantly enhanced the secretion of chondrogenic genes, including COL II and ACAN than that of the other groups. Moreover, 3DHAS showed less secretion of the COL I as compared to the other groups, even though differences were insignificant. In contrast, 2DS exhibited higher expression of COL X as compared to the 3D scaffold, indicating a hypertrophic phenotype of chondrocytes in 2DS. These results confirmed that 3DHAS can promote chondrogenesis while reduce the fibrosis and hypertrophy.

3.5. Regeneration of cartilage in nude mice

The feasibility of 3DS and 3DHAS to form neocartilage *in vivo* was discerned by implanting cell-scaffold constructs subcutaneously into the nude mice for up to 8 weeks. Both the 3DS and 3DHAS groups maintained their circular shapes and formed cartilage-like tissues with ivory-white appearance (Fig. 8A and E).

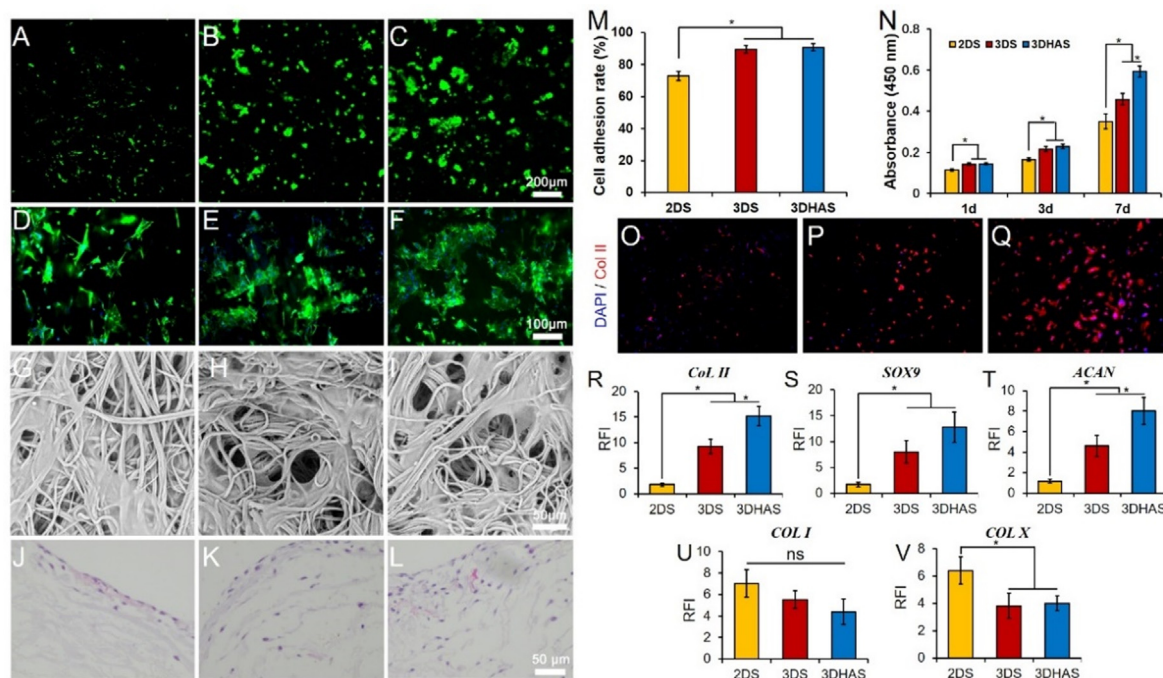


Fig. 7. Cell morphology and cell viability on different scaffolds. Live/dead assay of chondrocytes seeded on 2DS (A), 3DS (B), and 3DHAS (C) for up to 3 days (live and dead cells have been stained as green and red, respectively). Cytoskeletal staining of chondrocytes seeded on 2DS (D), 3DS (E), and 3DHAS (F) for up to 3 days (F-actin and nuclei were stained as green and blue, respectively). SEM images of the growth of chondrocytes on 2DS (G), 3DS (H), and 3DHAS (I) for up to 7 days. H&E staining of chondrocytes grown within 2DS (J), 3DS (K), and 3DHAS (L) for up to 7 days. (M) Cell adhesion rate of chondrocytes seeded on 2DS, 3DS, and 3DHAS for up to 4 h (* $p < 0.05$, $n = 3$). (N) Proliferation of chondrocytes on 2DS, 3DS, and 3DHAS at day 1, 3, and 7 (* $p < 0.05$, $n = 4$). Immunofluorescence staining of the collagen type II (red) and nuclei (blue) in the chondrocytes at day 14 on 2DS (O), 3DS (P), and 3DHAS (Q). Real-time PCR results of COL II (R), SOX9 (S), ACAN (T), COL I (U) and COL X (V) in the chondrocytes at day 14 on 2DS, 3DS, and 3DHAS (* $p < 0.05$, $n = 3$). RFI = Relative fold induction. (For interpretation of the references to color in this figure legend, the reader is referred to the web version of this article.)

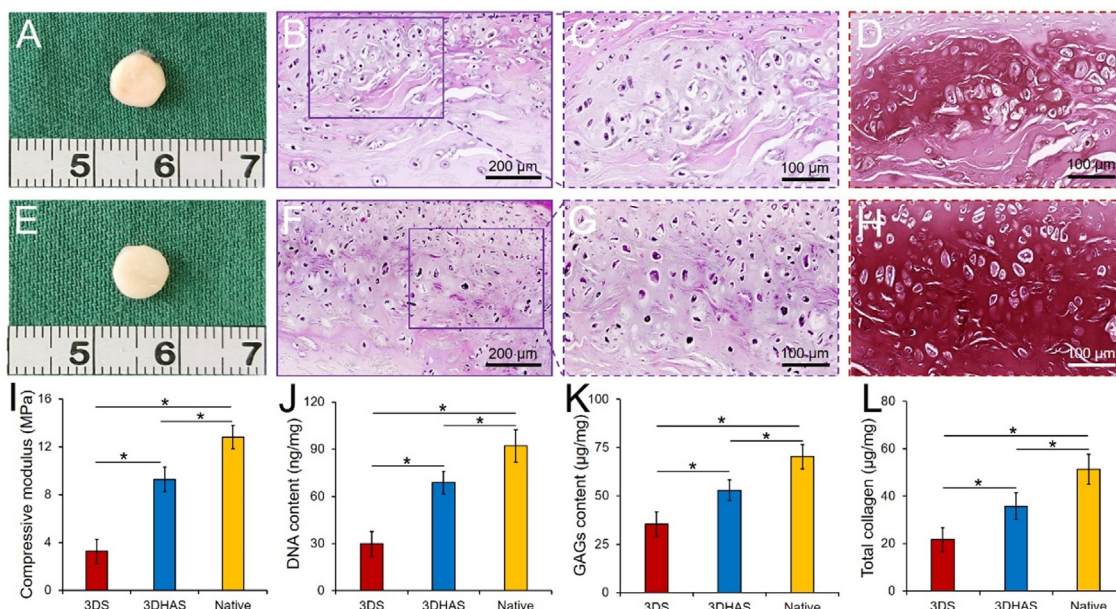


Fig. 8. A gross view and cartilage-specific staining of cell-scaffold constructs implanted subcutaneously in nude mice for up to 8 weeks. Macroscopic images, H&E staining, and Safranin-O staining of regenerated cartilage in 3DS (A-D) and 3DHAS (E-H) groups 8 weeks after subcutaneous implantation. Biomechanical and biochemical analyses of 3DS and 3DHAS engineered cartilage tissue *in vivo* including compressive modulus (I), DNA content (J), GAGs content (K), and total collagen content (L). Fresh auricular cartilage (native) was used as a control. (* $p < 0.05$, $n = 3$).

Histologically, the specimens in both groups led to the deposition of cartilage-specific ECM and typical lacuna of the cartilaginous tissues was observed. However, 3DS specimens (Fig. 8B-C) exhibited only a few channels and pores within the cell-scaffold construct as

compared to the dense regenerated tissues in 3DHAS (Fig. 8F-G). Moreover, samples in the 3DHAS group displayed a relatively uniform distribution of cartilaginous tissues as well as the deposition of the cartilage-specific matrix (Fig. 8H and Fig. S3C-D) as com-

pared to 3DS groups (Fig. 8D and Fig. S3A-B) as discerned by the positive staining of the Safranin-O and collagen type II. The biomechanical and biochemical results further indicated that the DNA, GAGs, collagen content, and compressive modulus of 3DHAS were higher than that of the 3DS, indicating more cell population and cartilage-specific matrix secretion in the *in-vivo*-engineered cartilage tissue within 3DHAS (Fig. 8I-L).

3.6. In situ articular cartilage regeneration in rabbits

The therapeutic potential of scaffolds for cartilage regeneration *in vivo* was also investigated in an articular cartilage defect model

in rabbits. The gross appearance at week 12 revealed cartilage defects in the non-treated groups. The 2DS groups displayed a visible boundary between the surrounding normal tissues and the defect region at week 12 after implantation (Fig. 9A-B). By contrast, a partially-filled defect was observed in the 3DS group (Fig. 9B). The defect site in the 3DHAS group exhibited a remarkable filling of the cartilage-like tissues with a smooth and a whitish articular surface (Fig. 9C).

H&E staining was performed to assess the structural integrity, hypocellularity, and fibrous tissue formation in the defect region. In the non-treated and 2DS groups, the defect border between the neotissues and adjacent cartilage tissues remained macroscop-

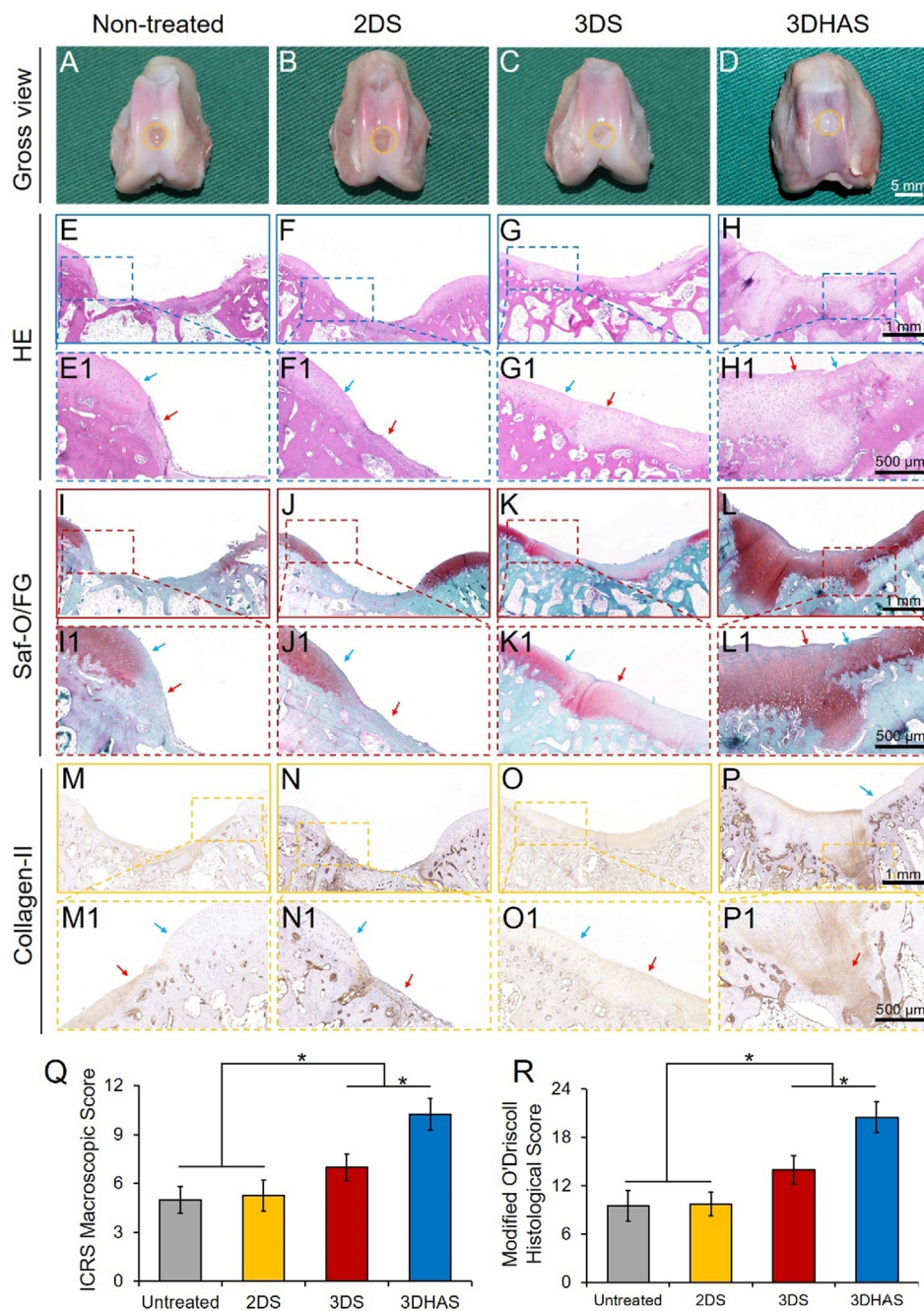


Fig. 9. Gross view and histological evaluation of the cartilage joints from non-treated, 2DS, 3DS, and 3DHAS groups 12 weeks after surgery. Macroscopic images of cartilage defects regions at 12 weeks (A – D) post-surgery, H&E (E – H, E1-H1), Safranin-O/FG staining (I – L, I1-L1) images of the repaired cartilage defects in different groups at 12 weeks after surgery. ICRS macroscopic assessment score (Q) and modified O’Driscoll histological score (R) of the repaired tissue (*p < 0.05, n = 4). Blue and red arrows indicate the intact cartilage the cartilage defect areas, respectively. (For interpretation of the references to color in this figure legend, the reader is referred to the web version of this article.)

ically visible and only a few fibrous tissues with unevenly distributed clustered cells grew and filled the defect (Fig. 9E-F, E1-F1). In the 3DS groups, a thin regenerated cartilage tissue was formed on the surface of defect; whereas some fibrous tissues and cartilage-like tissues were also identified (Fig. 9G and G1). However, the 3DHAS group exhibited a well-integrated morphology. Uniform cartilage-like tissue featured with lacunas and cell clusters were formed, which integrated well with the adjacent cartilage (Fig. 9H and H1). The irregular osteochondral interface of the 3DHAS could be attributed to the subsidence of the scaffold. During the operation, a stainless-steel punch was used to establish the defect model. Moreover, different thickness of the osteochondral layers of rabbits and the slight deviation in the position and depth of our punch might have accounted for the less regular osteochondral interface.

Safranin O-fast green and immunohistochemical staining of collagen type II were performed to assess the cellular matrix. The non-treated groups and 2DS groups did not exhibit staining for the collagen type II and Safranin O-fast green (Fig. 9I-J, I1-J1), indicating the lack of the GAGs and ECM deposition. By contrast, a thin regenerated cartilage tissue was formed on the defect surface of 3DS group which could be observed with weak staining of Safranin O-fast green (Fig. 9K and K1). However, the deposition of GAGs was intensively observed in 3DHAS 12 weeks post-implantation. It was observed that the numerous mature chondrocytes emerged on the surface of the defect, which demonstrated that the defect area was covered with abundant cartilage matrix (Fig. 9L and L1). The immunohistochemical analysis revealed only a limited deposition of the collagen type II in the non-treated groups (Fig. 9M and M1) and 2DS groups (Fig. 9N and N1). On the other hand, 3DS scaffolds showed a slight deposition of collagen type II (Fig. 9O and O1). The 3DHAS group revealed a significant deposition of the collagen type II (Fig. 9P and P1), indicating better ECM deposition in this group than that of the other groups. Moreover, it seems that type I collagen dominated the newborn cartilage matrix of non-treated (Fig. S4A and A1) and 2DS (Fig. S4B and B1) groups as well as some areas of 3DS groups (Fig. S4C and C1). In contrast, only a weak staining for the collagen type I was observed in 3DHAS (Fig. S4D and D1), indicating that the newborn cartilage in 3DHAS was similar to natural cartilage rather than fibrocartilage.

To further assess the reparative potential of each group, the corresponding ICRS macroscopic grading was performed and the obtained results are summarized in Fig. 9Q. The ICRS macroscopic score (a total 12 points) was highest in the 3DHAS groups (10.2 ± 0.9), followed by the 3DS group (7.0 ± 0.8), 2DS (5.2 ± 0.9), and non-treated group (5.0 ± 0.8) 12 weeks post-surgery. The modified O'Driscoll 24-point histological scoring also showed the similar trend (Fig. 9R), with 3DHAS gaining significantly higher score (20.5 ± 1.9) than that of the 3DS (14.0 ± 1.8), 2DS (9.7 ± 1.5), and non-treated groups (9.5 ± 1.9) 12-weeks post-implantation, respectively. These results indicate better repair in 3DHAS group than that of the 3DS, 2DS and the control group.

4. Discussion

As a robust method, electrospinning is commonly used for the fabrication of biomimetic scaffolds for various tissue engineering applications. However, the tightly-packed structure of normal electrospun membranes is unfavorable for the regeneration of the full-thickness cartilage. Significant efforts have been invested to afford 3D electrospun scaffolds with a stable 3D structure for cartilage repair [36,37]. However, the use of toxic organic solvents, lengthy procedure, and special manufacturing equipment hamper the clinical translation of electrospun scaffolds. The post-treatment of electrospun scaffolds is a viable approach to afford functional

scaffolds for tissue engineering. The gas foaming of electrospun scaffolds has been proposed to afford scaffolds with the high porosity and multilayered structure due to its simple, efficient and widely applicable features. However, several challenges should be addressed while accomplishing the gas foaming of electrospun scaffolds. The use of most of the scaffolds is restricted due to their weak mechanical properties, less bioactivity, and a prolonged inflammatory response *in vivo*, which is ascribed to their assembly from only a single type of polymer. Here, the biocompatibility and mechanical properties of the 3D gas foamed scaffolds were improved by the incorporation of SF and crosslinking with the HA. To the best of the authors knowledge, the gas foamed HA-crosslinked PLCL/SF scaffolds have yet not been employed for the regeneration of the articular cartilage. Hyaluronic acid cross-linked 3D scaffolds showed promising results than that of the scaffolds devoid of the HA.

The choice of materials and the structural stability are central for the preparation of 3D gas foamed scaffolds. 2D nanofibrous membranes composed of PLCL and SF were fabricated by using DLS electrospinning system. The addition of the SF has been previously demonstrated to improve the hydrophilicity and cytocompatibility of the hybrid nanostructures [38]. Parallely, mechano-elastic and biodegradable PLCL imparts mechanical stability to the scaffolds. Consequently, PLCL/SF hybrid scaffolds have been extensively researched for tissue engineering applications, including nerve, tendon, and blood vessel regeneration [39]. Despite these improvements in the physico-chemical properties and the biocompatibility, the nanoyarn scaffolds offer only a marginal benefit for CTE, plausibly due to their small thickness, monotonous composition, and poor mechanical properties. Besides, nanoyarn scaffolds may be collapsed during the gas foaming process. This necessitates the crosslinking of the 2D mats to afford a stable morphology, especially those containing natural water-soluble proteins. Glutaraldehyde or EDC/NHS are commonly used as crosslinking agents for protein-based materials. Amongst, the EDC/NHS was chosen as a crosslinking agent due to its low cytotoxicity [26]. However, simply cross-linked PLCL/SF scaffolds could not meet the requirements for the optimal cartilage regeneration due to the lack of bioactivity. HA, a natural glycosaminoglycan and one of the components of articular cartilage, has been shown to specifically interact with the growing cells, which has been widely exploited for CTE [40]. Consequently, nanoyarn scaffolds were crosslinked with the HA to improve their mechanical properties and bioactivity. After the subsequent gas foaming, none of the 3D scaffolds collapsed and all of scaffolds remained intact similar to their original 3D shape after lyophilization, which suggested the successful fabrication of 3D scaffolds with interconnected networks and a stable 3D-like morphology.

Hydrophilicity is a key parameter to afford gas foamed scaffolds. 2D nanoyarn containing mats fabricated by DLS electrospinning system exhibit improved hydrophilicity as compared to the normal 2D flat electrospun membranes [8] thus accelerating the foaming efficiency. Once the scaffold contacts with the foaming solution, the foaming agent instantly absorbs into the whole scaffold. Then, NaBH_4 solution produces H_2 bubbles *in situ*, which penetrate into the scaffold and continuously exert pressure on the surrounding nanofibers, thus increasing the thickness and porosity of flat mats. Noticeably, the concentration of the foaming agent used in this study was 0.1 M, which is economical and did not suppress the foaming rate, justifying the superiority of choosing nanoyarn containing mats to fabricate 3D scaffolds. The thickness of the 3D scaffold can further be controlled by adjusting the foaming time, which allows for the customization of different-sized scaffolds according to various kinds of cartilage injuries.

3D gas foamed scaffolds exhibited preserved nanotopographical cues and orientation of nanofibers, which may further help

orchestrate the regenerative response as topographic cues have been demonstrated to instruct the cell behavior and morphology [41]. Jia et al. reported that the aligned nanofibers promote the pro-healing phenotype in macrophages, resulting in a marked progress in tissue regeneration [42]. Moreover, the preserved aligned morphology in 3D scaffolds may help achieve better cell–cell communication and cartilage defect healing.

After freeze-drying, the pore area and porosity of scaffolds were increased due to the release of the trapped bubbles from the frozen scaffolds. Large gap distances and multi-layered structures could be observed in the 3D gas foamed scaffolds. The large pores and the high porosity improves the diffusion of oxygen and nutrients, removes waste products, and allows cellular infiltration into the scaffold [43]. It has indeed been established that the high porosity induces macrophage polarization toward the M2 phenotype, promoting wound healing and modulating the foreign body response [38]. Since articular cartilage injury is often accompanied by an inflammatory response, a porous scaffold may also alleviate the inflammation. Moreover, high porosity also results into superior water absorption capacity of 3D scaffold for mimicking the resilience and lubrication of the joint. The cellular fibrous networks, often found in nature, such as spider webs and honeycombs, are highly helpful to maximize cellular-specific mechanical strength [44]. The previously proposed principles for the fibrous freeze-shaping process can be extended to explain the formation of honeycomb-like nanofiber structure [45]. The existence of fibrous network strengthens the connection between layers within 3DHAS, thus forming a stable structure.

The appropriate mechanical strength is critical for the success of the scaffolds. An optimal 3D scaffold is expected to withstand the specific load and maintain the overall mechanical performance. We have observed improved biomechanical properties of scaffolds after cross-linking with the HA. 3DHAS scaffolds have also shown higher modulus with less stress loss under multiple loading–unloading cycles than that of the 3DS; which may be due to the stronger hydrogen bonding between the fibrous network of HA as well as the formation of amide bonds between the amino groups and the carboxylic groups. Moreover, for up to a certain extent, the bound nanoyarns within the scaffolds may also contribute to the improved mechanical stability. Overall, the enhanced mechanical strength may be helpful to afford a stable 3D-like environment for the growth of the chondrocytes and cartilage tissue regeneration [11].

The fundamental requirement for biomaterials is the biocompatibility. The gas foamed 3D scaffolds displayed good blood compatibility and blood absorption capacity, which can be ascribed to the formation of the layered structures, as it may provide more space for the interaction of the blood with the nanofiber scaffolds. Moreover, the amino groups in SF may interact with the negative charge of the platelets to accelerate hemostasis [21]. Hemolysis ratio is defined as the degree of erythrolysis by the blood contacting material which disrupts erythrocytes' membrane and releases hemoglobin into the plasma [46,47]. All of the scaffolds demonstrated a low hemolysis ratio, highlighting their potential application in blood contacting devices. The biocompatibility of the scaffolds was also evaluated by *in vitro* cell culture. Expanded porous constructs consisting of aligned fibers are invaluable to provide cell adhesive and cell chemotactic cues [48]. Thus, 3D scaffolds were superior to enhance cell adhesion, proliferation, and infiltration than that of 2DS. It has previously been deciphered that the HA provides physiochemical and pharmacological functions, including scavenging reactive oxygen species (ROS) as well as inhibiting adhesion of immune complexes to polymorphonuclear cells and the migration and accumulation of leukocytes and macrophages, which may collectively confer the additional chondroprotective effects [49,50]. A previous study showed that the

proliferation of chondrocytes as well as the deposition of glycosaminoglycans (GAGs) was increased with the addition of HA into collagen gels [51]. Cell surface glycoprotein (CD44) may interact with the HA and improve biochemical interactions with chondrocytes [52]. Thus, HA-crosslinked 3DHAS scaffolds are superior to the 3DS in promoting cell proliferation, which may also promote the expression of chondrocytes-associated specific proteins. Although cell adhesion to biomaterials facilitates cell survival and proliferation, cytoskeletal tension within chondrocytes is responsible for dedifferentiation and phenotypical change to fibroblast-like morphology. Thus, the expression of the collagen type I was increased in all of the scaffolds compared to day 0. However, 3DHAS exhibited partially lowered expression of fibrotic genes and substantially higher expression of cartilage-specific genes as compared to 2DS and 3DS. Conventional 2D thin-layer culture is considered unsuitable, which does not support the chondrogenic phenotype during cell culture *in vitro*. In contrast, it is well-known that the 3D culture not only help maintain the phenotype of chondrocytes but also promote the differentiation of articular chondrocytes [53,54]. Furthermore, being a component of the cartilage ECM, HA can promote chondrogenesis. Therefore, 3DHAS provide cartilage-like microenvironment for the maintenance of chondrogenic phenotypes.

An ideal scaffold should promote both the cell growth and tissue regeneration. In the current study, the cell-scaffold constructs of both 3DS and 3DHAS groups formed regenerated neocartilage 8 weeks after subcutaneous implantation. The underlying mechanism is that the multi-layered structures and interconnected networks are beneficial for the infiltration of cells and the diffusion of nutrients, and the living bioreactor (nude mice) possesses an excellent microenvironment for cartilage regeneration *in vivo*. The feasibility to repair an articular cartilage defect is also an important indicator for the clinical translation of 3D scaffolds. Notably, the results of the subcutaneous and articular cartilage implantation suggest that 3DHAS form uniform cartilage-like tissues along with the regeneration of mature cartilage-like tissues and the secretion of the cartilaginous matrix *in vivo*. This may be ascribed to the reason that the HA cross-linked scaffolds possess native cartilage-like composition, leading to good biocompatibility between the chondrocytes and the scaffolds as described above. Thus, more host cells were recruited, promoting the secretion of cartilage ECM and accelerating the cartilage repair *in vivo*.

5. Conclusions

In conclusion, we have fabricated novel 3D HA-crosslinked porous nanofibrous scaffolds via treatment with a gas foaming agent and subsequent freeze-drying. For the first time, gas foamed electrospun scaffolds were evaluated for the regeneration of the articular cartilage. 3D gas foamed scaffolds exhibited low density, large pore area, high porosity, excellent water absorption capacity and mechanical stability. Moreover, they preserved nanotopographical architecture and showed multilayered structures. All of the scaffolds exhibited good hemocompatibility and cytocompatibility. Most importantly, the bioactivity of the scaffolds was improved by crosslinking with the HA. Further study revealed that 3DHAS displayed better ability for the proliferation of chondrocytes than that of the other groups and a higher expression of cartilage-specific genes to support the chondrogenic phenotype *in vitro*. The 3DHAS achieved satisfactory cartilage regeneration in a subcutaneous implantation in nude mice as well as significant repair of the cartilage defects in rabbits. The current study proposes a promising cartilage ECM-mimicking 3D porous scaffold for the regeneration of the articular cartilage. Further research will be aimed at improving the accurate control of scaffold' aperture,

accelerating cartilage maturation and matrix secretion, and ultimately achieving optimal engineered cartilage functions.

CRedit authorship contribution statement

Yujie Chen: Investigation, Methodology, Formal analysis, Writing - original draft. **Wei Xu:** Investigation, Conceptualization, Data curation. **Muhammad Shafiq:** Conceptualization, Writing - review & editing. **Jincheng Tang:** Conceptualization, Data curation. **Junxiang Hao:** Conceptualization, Data curation. **Xianrui Xie:** Investigation, Conceptualization. **Zhengchao Yuan:** Conceptualization, Data curation. **Xianghao Xiao:** Investigation, Conceptualization. **Yu Liu:** Conceptualization, Funding acquisition, Writing - review & editing. **Xiumei Mo:** Supervision, Funding acquisition, Writing - review & editing.

Declaration of Competing Interest

The authors declare that they have no known competing financial interests or personal relationships that could have appeared to influence the work reported in this paper.

Acknowledgement

This research was supported by the Fundamental Research Funds for the Central Universities (2232019A3-07), National Key Research Program of China (2016YFA0201702 of 2016YFA0201700), National Nature Science Foundation of China (No. 32050410286, 31771023, 3201101259), Science and Technology Commission of Shanghai Municipality (No.19441902600, 20S31900900, 20DZ2254900), the Fundamental Research Funds for the Central Universities and Graduate Student Innovation Fund of Donghua University (No. CUSF-DH-D-2020061), Program of Shanghai Academic/Technology Research Leader (19XD1431100), and Sino German Science Foundation Research Exchange Center (M-0263).

Appendix A. Supplementary data

Supplementary data to this article can be found online at <https://doi.org/10.1016/j.jcis.2021.06.067>.

References

- W. Wei, Y. Ma, X. Yao, W. Zhou, X. Wang, C. Li, J. Lin, Q. He, S. Leptihn, H. Ouyang, Advanced hydrogels for the repair of cartilage defects and regeneration, *Bioact. Mater.* 6 (2021) 998–1011, <https://doi.org/10.1016/j.bioactmat.2020.09.030>.
- E.A. Makris, A.H. Gomoll, K.N. Malizos, J.C. Hu, K.A. Athanasiou, Repair and tissue engineering techniques for articular cartilage, *Nat. Rev. Rheumatol.* 11 (2015) 21–34, <https://doi.org/10.1038/nrrheum.2014.157>.
- A.R. Armiento, M.J. Stoddart, M. Alini, D. Eglin, Biomaterials for articular cartilage tissue engineering: Learning from biology, *Acta Biomater.* 65 (2018) 1–20, <https://doi.org/10.1016/j.actbio.2017.11.021>.
- D.J. Huey, J.C. Hu, K.A. Athanasiou, Remains elusive, *Science* (80-) 6933 (2012) 917–921, <https://doi.org/10.1126/science.1222454>.
- Y. Chen, M. Sha, M. Liu, Y. Morsi, X. Mo, Advanced fabrication for electrospun three-dimensional nanofiber aerogels and scaffolds, *Bioact. Mater.* 5 (2020) 963–979, <https://doi.org/10.1016/j.bioactmat.2020.06.023>.
- K. Zhang, N. Cao, X. Guo, Q. Zou, S. Zhou, R. Yang, W. Zhao, X. Mo, W. Liu, Q. Fu, The fabrication of 3D surface scaffold of collagen/poly (L-lactide-co-caprolactone) with dynamic liquid system and its application in urinary incontinence treatment as a tissue engineered sub-urethral sling: In vitro and in vivo study, *NeuroUrol. Urodyn.* 37 (2018) 978–985, <https://doi.org/10.1002/nau.23438>.
- K. Zhang, X. Guo, Y. Li, Q. Fu, X. Mo, K. Nelson, W. Zhao, Electrospun nanoyarn seeded with myoblasts induced from placental stem cells for the application of stress urinary incontinence sling: An in vitro study, *Colloids Surfaces B Biointerfaces.* 144 (2016) 21–32, <https://doi.org/10.1016/j.colsurfb.2016.03.083>.
- T. Wu, J. Zhang, Y. Wang, B. Sun, X. Guo, Y. Morsi, H. El-Hamshary, M. El-Newehy, X. Mo, Development of dynamic liquid and conjugated electrospun poly(L-lactide-co-caprolactone)/collagen nanoyarns for regulating vascular smooth muscle cells growth, *J. Biomed. Nanotechnol.* 13 (2017) 303–312, <https://doi.org/10.1166/jbn.2017.2352>.
- Y. Si, J. Yu, X. Tang, J. Ge, B. Ding, Ultralight nanofiber-assembled cellular aerogels with superelasticity and multifunctionality, *Nat. Commun.* 5 (2014) 5802, <https://doi.org/10.1038/ncomms6802>.
- Y. Si, X. Wang, C. Yan, L. Yang, J. Yu, B. Ding, Ultralight biomass-derived carbonaceous nanofibrous aerogels with superelasticity and high pressure-sensitivity, *Adv. Mater.* 28 (2016) 9512–9518, <https://doi.org/10.1002/adma.201603143>.
- W. Chen, Y. Xu, Y. Li, L. Jia, X. Mo, G. Jiang, G. Zhou, 3D printing electrospinning fiber-reinforced decellularized extracellular matrix for cartilage regeneration, *Chem. Eng. J.* (2019), <https://doi.org/10.1016/j.cej.2019.122986>.
- S.K. Boda, S. Chen, K. Chu, H.J. Kim, J. Xie, Electrospinning electrospun nanofiber segments into injectable microspheres for potential cell delivery, *ACS Appl. Mater. Interfaces.* 10 (2018) 25069–25079, <https://doi.org/10.1021/acsami.8b06386>.
- J. Song, G. Zhu, H. Gao, L. Wang, N. Li, X. Shi, Y. Wang, Origami meets electrospinning: a new strategy for 3D nanofiber scaffolds, *Bio-Design Manuf.* 1 (2018) 254–264, <https://doi.org/10.1007/s42242-018-0027-9>.
- J. Jiang, S. Chen, H. Wang, M.A. Carlson, A.F. Gombart, J. Xie, CO₂-expanded nanofiber scaffolds maintain activity of encapsulated bioactive materials and promote cellular infiltration and positive host response, *Acta Biomater.* 68 (2018) 237–248, <https://doi.org/10.1016/j.actbio.2017.12.018>.
- J. Jiang, M.A. Carlson, M.J. Teusink, H. Wang, M.R. MacEwan, J. Xie, Expanding two-dimensional electrospun nanofiber membranes in the third dimension by a modified gas-foaming technique, *ACS Biomater. Sci. Eng.* 1 (2015) 991–1001, <https://doi.org/10.1021/acsbiomaterials.5b00238>.
- S.E. Kim, A.P. Tiwari, Three dimensional polycaprolactone/cellulose scaffold containing calcium-based particles: a new platform for bone regeneration, *Carbohydr. Polym.* 250 (2020), <https://doi.org/10.1016/j.carbpol.2020.116880>.
- J. Jiang, Z. Li, H. Wang, Y. Wang, M.A. Carlson, M.J. Teusink, M.R. MacEwan, L. Gu, J. Xie, Expanded 3D nanofiber scaffolds: cell penetration, neovascularization, and host response, *Adv. Healthc. Mater.* 5 (2016) 2993–3003, <https://doi.org/10.1002/adhm.201600808>.
- X. Wang, B. Ding, B. Li, Biomimetic electrospun nanofiber structures for tissue engineering, *Mater. Today.* 16 (2013) 229–241, <https://doi.org/10.1016/j.mattod.2013.06.005>.
- M.K. Joshi, H.R. Pant, A.P. Tiwari, H.J. Kim, C.H. Park, C.S. Kim, Multi-layered macroporous three-dimensional nanofibrous scaffold via a novel gas foaming technique, *Chem. Eng. J.* 275 (2015) 79–88, <https://doi.org/10.1016/j.cej.2015.03.121>.
- X. Jing, H. Li, H.Y. Mi, Y.J. Liu, Y.M. Tan, Fabrication of fluffy shish-kebab structured nanofibers by electrospinning, CO₂ escaping foaming and controlled crystallization for biomimetic tissue engineering scaffolds, *Chem. Eng. J.* 372 (2019) 785–795, <https://doi.org/10.1016/j.cej.2019.04.194>.
- K. Zhang, X. Bai, Z. Yuan, X. Cao, X. Jiao, Y. Li, Y. Qin, Y. Wen, X. Zhang, Layered nanofiber sponge with an improved capacity for promoting blood coagulation and wound healing, *Biomaterials.* 204 (2019) 70–79, <https://doi.org/10.1016/j.biomaterials.2019.03.008>.
- F. Rao, Z. Yuan, M. Li, F. Yu, X. Fang, B. Jiang, Y. Wen, P. Zhang, Expanded 3D nanofiber sponge scaffolds by gas-foaming technique enhance peripheral nerve regeneration, *Artif. Cells, Nanomedicine, Biotechnol.* 47 (2019) 491–500, <https://doi.org/10.1080/21691401.2018.1557669>.
- J. Chen, J. Yang, L. Wang, X. Zhang, B.C. Heng, D.-A. Wang, Z. Ge, Modified hyaluronic acid hydrogels with chemical groups that facilitate adhesion to host tissues enhance cartilage regeneration, *Bioact. Mater.* 6 (2021) 1689–1698, <https://doi.org/10.1016/j.bioactmat.2020.11.020>.
- W.S. Toh, T.C. Lim, M. Kurisawa, M. Spector, Modulation of mesenchymal stem cell chondrogenesis in a tunable hyaluronic acid hydrogel microenvironment, *Biomaterials.* 33 (2012) 3835–3845, <https://doi.org/10.1016/j.biomaterials.2012.01.065>.
- S.K. Seidlits, C.T. Drinnan, R.R. Petersen, J.B. Shear, L.J. Suggs, C.E. Schmidt, Fibronectin-hyaluronic acid composite hydrogels for three-dimensional endothelial cell culture, *Acta Biomater.* 7 (2011) 2401–2409, <https://doi.org/10.1016/j.actbio.2011.03.024>.
- W. Chen, S. Chen, Y. Morsi, H. El-Hamshary, M. El-Newehy, C. Fan, X. Mo, Superabsorbent 3D scaffold based on electrospun nanofibers for cartilage tissue engineering, *ACS Appl. Mater. Interfaces.* 8 (2016) 24415–24425, <https://doi.org/10.1021/acsami.6b06825>.
- B. Sun, J. Li, W. Liu, B.M. Aqeel, H. El-Hamshary, S.S. Al-Deyab, X. Mo, Fabrication and characterization of mineralized P(LLA-CL)/SF three-dimensional nanoyarn scaffolds, *Iran. Polym. J. (English Ed.)* 24 (2014) 29–40, <https://doi.org/10.1007/s13726-014-0297-9>.
- Y. Xu, D. Li, Z. Yin, A. He, M. Lin, G. Jiang, X. Song, X. Hu, Y. Liu, J. Wang, X. Wang, L. Duan, G. Zhou, Tissue-engineered trachea regeneration using decellularized trachea matrix treated with laser microprobe technique, *Acta Biomater.* 58 (2017) 113–121, <https://doi.org/10.1016/j.actbio.2017.05.010>.
- D. Yan, G. Zhou, X. Zhou, W. Liu, W.J. Zhang, X. Luo, L. Zhang, T. Jiang, L. Cui, Y. Cao, The impact of low levels of collagen IX and pyridinoline on the mechanical properties of in vitro engineered cartilage, *Biomaterials.* 30 (2009) 814–821, <https://doi.org/10.1016/j.biomaterials.2008.10.042>.

- [30] G. Kesava Reddy, C.S. Enwemeka, A simplified method for the analysis of hydroxyproline in biological tissues, *Clin. Biochem.* 29 (1996) 225–229, [https://doi.org/10.1016/0009-9120\(96\)00003-6](https://doi.org/10.1016/0009-9120(96)00003-6).
- [31] W. Yu, R. Wanka, J.A. Finlay, J.L. Clarke, A.S. Clare, A. Rosenhahn, Degradable hyaluronic acid/chitosan polyelectrolyte multilayers with marine fouling-release properties, *Biofouling*. (2020) 1–22, <https://doi.org/10.1080/08927014.2020.1846725>.
- [32] K. Lewandowska, Miscibility studies of hyaluronic acid and poly(Vinyl alcohol) blends in various solvents, *Materials (Basel)*. 13 (2020) 1–12, <https://doi.org/10.3390/ma13214750>.
- [33] K. Zhang, X. Mo, C. Huang, C. He, H. Wang, Electrospun scaffolds from silk fibroin and their cellular compatibility, *J. Biomed. Mater. Res. - Part A*. 93 (2010) 976–983, <https://doi.org/10.1002/jbm.a.32497>.
- [34] J. Almodóvar, L.W. Place, J. Gogolski, K. Erickson, M.J. Kipper, Layer-by-layer assembly of polysaccharide-based polyelectrolyte multilayers: A spectroscopic study of hydrophilicity, composition, and ion pairing, *Biomacromolecules*. 12 (2011) 2755–2765, <https://doi.org/10.1021/bm200519y>.
- [35] X. Chen, J. Wang, Q. An, D. Li, P. Liu, W. Zhu, X. Mo, Electrospun poly(l-lactic acid-co-ε-caprolactone) fibers loaded with heparin and vascular endothelial growth factor to improve blood compatibility and endothelial progenitor cell proliferation, *Colloids Surfaces B Biointerfaces*. 128 (2015) 106–114, <https://doi.org/10.1016/j.colsurfb.2015.02.023>.
- [36] Y. Li, Y. Liu, X. Xun, W. Zhang, Y. Xu, D. Gu, Three-dimensional porous scaffolds with biomimetic microarchitecture and bioactivity for cartilage tissue engineering, *ACS Appl. Mater. Interfaces*. 11 (2019) 36359–36370, <https://doi.org/10.1021/acsami.9b12206>.
- [37] W. Chen, Y. Xu, Y. Liu, Z. Wang, Y. Li, G. Jiang, X. Mo, G. Zhou, Three-dimensional printed electrospun fiber-based scaffold for cartilage regeneration, *Mater. Des.* 179 (2019), <https://doi.org/10.1016/j.matdes.2019.107886> 107886.
- [38] Y. Chen, Z. Jia, M. Shafiq, X. Xie, X. Xiao, R. Castro, J. Rodrigues, J. Wu, G. Zhou, X. Mo, Gas foaming of electrospun poly(L-lactide-co-caprolactone)/silk fibroin nanofiber scaffolds to promote cellular infiltration and tissue regeneration, *Colloids Surfaces B Biointerfaces*. 201 (2021), <https://doi.org/10.1016/j.colsurfb.2021.111637> 111637.
- [39] X. Xie, Y. Chen, X. Wang, X. Xu, Y. Shen, A. ur R. Khan, A. Aldabahi, A.E. Fetz, G. L. Bowlin, M. El-Newehy, X. Mo, Electrospinning nanofiber scaffolds for soft and hard tissue regeneration, *J. Mater. Sci. Technol.* 59 (2020) 243–261, <https://doi.org/10.1016/j.jmst.2020.04.037>.
- [40] M.N. Collins, C. Birkinshaw, Hyaluronic acid based scaffolds for tissue engineering - A review, *Carbohydr. Polym.* 92 (2013) 1262–1279, <https://doi.org/10.1016/j.carbpol.2012.10.028>.
- [41] R.V. Bellamkonda, Peripheral nerve regeneration: An opinion on channels, scaffolds and anisotropy, *Biomaterials*. 27 (2006) 3515–3518, <https://doi.org/10.1016/j.biomaterials.2006.02.030>.
- [42] Y. Jia, W. Yang, K. Zhang, S. Qiu, J. Xu, C. Wang, Y. Chai, Nanofiber arrangement regulates peripheral nerve regeneration through differential modulation of macrophage phenotypes, *Acta Biomater.* 83 (2019) 291–301, <https://doi.org/10.1016/j.actbio.2018.10.040>.
- [43] N. Davidenko, J.J. Campbell, E.S. Thian, C.J. Watson, R.E. Cameron, Collagen-hyaluronic acid scaffolds for adipose tissue engineering, *Acta Biomater.* 6 (2010) 3957–3968, <https://doi.org/10.1016/j.actbio.2010.05.005>.
- [44] Y. Si, L. Wang, X. Wang, N. Tang, J. Yu, B. Ding, Ultrahigh-water-content, superelastic, and shape-memory nanofiber-assembled hydrogels exhibiting pressure-responsive conductivity, *Adv. Mater.* 29 (2017) 1–7, <https://doi.org/10.1002/adma.201700339>.
- [45] L. Qiu, J.Z. Liu, S.L.Y. Chang, Y. Wu, D. Li, Biomimetic superelastic graphene-based cellular monoliths, *Nat. Commun.* 3 (2012) 1–7, <https://doi.org/10.1038/ncomms2251>.
- [46] N. Cai, Q. Li, J. Zhang, T. Xu, W. Zhao, J. Yang, L. Zhang, Antifouling zwitterionic hydrogel coating improves hemocompatibility of activated carbon hemoabsorbent, *J. Colloid Interface Sci.* 503 (2017) 168–177, <https://doi.org/10.1016/j.jcis.2017.04.024>.
- [47] M. Shafiq, D. Kong, S.H. Kim, SDF-1α peptide tethered polyester facilitates tissue repair by endogenous cell mobilization and recruitment, *J. Biomed. Mater. Res. - Part A*. 105 (2017) 2670–2684, <https://doi.org/10.1002/jbm.a.36130>.
- [48] S. Patel, K. Kurpinski, R. Quigley, H. Gao, B.S. Hsiao, M.M. Poo, S. Li, Bioactive nanofibers: Synergistic effects of nanotopography and chemical signaling on cell guidance, *Nano Lett.* 7 (2007) 2122–2128, <https://doi.org/10.1021/nl071182z>.
- [49] J. Hauptstein, T. Böck, M. Bartolf-Kopp, L. Forster, P. Stahlhut, A. Nadernezhad, G. Blahetek, A. Zerneck-Madsen, R. Detsch, T. Jüngst, J. Groll, J. Teßmar, T. Blunk, Hyaluronic acid-based bioink composition enabling 3D bioprinting and improving quality of deposited cartilaginous extracellular matrix, *Adv. Healthc. Mater.* 9 (2020) 1–15, <https://doi.org/10.1002/adhm.202000737>.
- [50] M. Akmal, A. Singh, A. Anand, A. Kesani, N. Aslam, A. Goodship, G. Bentley, The effects of hyaluronic acid on articular chondrocytes, *J. Bone Jt. Surg. - Ser. B*. 87 (2005) 1143–1149, <https://doi.org/10.1302/0301-620X.87B8.15083>.
- [51] K. Kawasaki, M. Ochi, Y. Uchio, N. Adachi, M. Matsusaki, Hyaluronic acid enhances proliferation and chondroitin sulfate synthesis in cultured chondrocytes embedded in collagen gels, *J. Cell. Physiol.* 179 (1999) 142–148, [https://doi.org/10.1002/\(SICI\)1097-4652\(199905\)179:2<142::AID-JCP4>3.0.CO;2-Q](https://doi.org/10.1002/(SICI)1097-4652(199905)179:2<142::AID-JCP4>3.0.CO;2-Q).
- [52] G. Chow, C.B. Knudson, G. Homandberg, W. Knudson, Increased expression of CD44 in bovine articular chondrocytes by catabolic cellular mediators, *J. Biol. Chem.* 270 (1995) 27734–27741, <https://doi.org/10.1074/jbc.270.46.27734>.
- [53] K.R. Brodtkin, A.J. García, M.E. Levenston, Chondrocyte phenotypes on different extracellular matrix monolayers, *Biomaterials*. 25 (2004) 5929–5938, <https://doi.org/10.1016/j.biomaterials.2004.01.044>.
- [54] Z. Lin, C. Willers, J. Xu, M.H. Zheng, The chondrocyte: Biology and clinical application, *Tissue Eng.* 12 (2006) 1971–1984, <https://doi.org/10.1089/ten.2006.12.1971>.